Sparse grid reconstructions for Particle-In-Cell methods

Fabrice Deluzet, Gwenael Fubiani, Laurent Garrigues, Clément Guillet, Jacek Narski

SPARSE GRID RECONSTRUCTIONS FOR PARTICLE-IN-CELL METHODS

F. DELUZET[†], G. FUBIANI[‡], L. GARRIGUES[‡], C. GUILLET[†‡⋆], AND J. NARSKI[†]

Abstract. In this article, we propose and analyse Particle-In-Cell (PIC) methods embedding sparse grid reconstruction as those introduced in [1, 2]. The sparse grid reconstructions offer a significant improvement on the statistical error of PIC schemes as well as a reduction in the complexity of the problem providing the electric field. Main results on the convergence of the electric field interpolant and conservation properties are provided in this paper. Besides, tailored sparse grid reconstructions, in the frame of the offset combination technique, are proposed to introduce PIC methods with improved efficiency. The methods are assessed numerically and compared to existing PIC schemes thanks to classical benchmarks with remarkable prospects for three dimensional computations.

Keywords. Plasma physics, Particle-In-Cell (PIC), sparse grids, combination technique

1. Introduction

Particle-In-Cell (PIC) discretizations have been among the most used numerical methods in the simulation of kinetic plasmas for years [3, 4, 5, 6] and is still topical [7, 8, 9, 10]. The method consists in a coupling between a Lagrangian method for the Vlasov equation, based on the integration of numerical particle trajectories and, a mesh-based discretization of Poisson's equation (or Maxwell's system) for the computation of the self-consistent field. Despite their simplicity, ease of parallelization and robustness, Particle-In-Cell schemes still contain a significant drawback: the statistical error originating from the sampling of the distribution function by numerical particles. This numerical noise decreases slowly with the increase of the average number of particles per cell. Therefore, a large number of particles may be required, necessitating tremendous computational resources, specifically for three dimensional simulations for which the desire precision may impose a number of cells as large as 10^9, the number of particles exceeding 10^{12}. Noise reduction strategies aim at maintaining the accuracy of computations with a reduced set of particles, they have therefore received a lot of attention with, for instance, variance reduction methods such as the δf method [11] or the quiet start initialization procedure [6] as well as filtering methods in either Fourier [12] or wavelet domain [13].

[†] Université de Toulouse; UPS, INSA, UT1, UTM,, Institut de Mathématiques de Toulouse,, CNRS, Institut de Mathématiques de Toulouse UMR 5219,, F-31062 Toulouse, France

[‡]LAPLACE, Université de Toulouse, CNRS, INPT, UPS,, 118 Route de Narbonne, 31062 Toulouse, France

[⋆] Corrresponding author

Sparse grid methods [14, 15], originally developed for the interpolation of high dimensional functions, then extended to the approximation of partial differential equations [16, 17, 18, 19], have recently been applied, in the framework of the so-called combination technique [20, 21], to Particle-In-Cell schemes [1, 2, 22, 23, 24]. The aim here is to improve the properties of PIC methods with respect to the statistical error resulting from the particle sampling. In the sparse grid reconstructions, the numerical approximation are recomposed from partial representations carried out on a hierarchy of sparse grids with coarse resolutions. Compared to a regular Cartesian grid, the mean number of particles per cell is larger for any of the sparse grids. This crucial feature offers either a mitigation of the statistical noise or a decrease of the total number of numerical particles for a precision comparable to standard PIC discretizations. Besides, considering the thorough studies conducted during recent years to apply the combination technique to the resolution of PDEs, promising improvements in the computational efficiency are expected for the resolution of Poisson's equation (see [25, 21, 26]) providing the electric field in the Particle-In-Cell framework. These gains are specifically substantial for three dimensional applications.

The objective of the present paper is to provide an overview of the existing Particle-In-Cell discretizations implementing the sparse grid combination technique, to conduct a formal analysis to explain their merits and weaknesses and support the development of new methods with improved efficiency. The results provided herein are limited to two dimensional geometries. Nonetheless, they are readily extendibles to an arbitrary number of dimensions, using the same tools, however with an additional complexity of notation avoided within the present document.

The analyses of standard as well as sparse grid PIC discretizations unravel that, for both methods, the approximation error may be decomposed into three contributions. The precision of the methods is characterized by the accuracy of the most probable value of the statistics associated to the particle sampling, this component being referred to as the bias. This is a grid-based error related to both the mesh size (h) and the smoothness of the solution with a component, denoted $\mathcal{G}_n^{\|}$, depending on the solution non-cross derivatives and, another contribution, $\mathcal{G}_n^{\times}$, depending on cross derivatives. The last error component, $\mathcal{P}_{n,N}$, is the so-called numerical noise or particle sampling error, providing the magnitude of the dispersion of the values attached to a sample of particles. The introduction of sparse grid reconstructions within PIC discretizations entails an increase of the grid error, specifically $\mathcal{G}_n^{\times}$ together with a significant mitigation of the statistical noise. This outlines the potential of these approaches: sparse grid reconstructions may be tailored to define different trades-off between the components of the error and finally mitigate the most detrimental one for the precision of PIC numerical approximations (the statistical noise). This leads to the derivation of the new sparse-grid methods introduced herein, with an improved numerical efficiency. The analyses conducted in this paper are also aimed at demonstrating the convergence of the electric field sparse grid interpolant. This is a major contribution of the paper since no convergence properties have already been proposed so far for this quantity.

The paper is organized as follows. In section 2, the Particle-In-Cell scheme is outlined in its conventional framework with the definition of the grid-based and the particle sampling errors. In section 3.1, sparse grids approximations are introduced

in the specific framework of the combination technique before being merged with Particle-In-Cell methods in section 3.2. In section 3.3, a generalization of the combination technique, referred to as offset combination technique, is proposed in order to tune the trade-off between the different components of the sparse grid approximation error of the distribution function moment interpolant. Section 3.4 is devoted to the introduction of two enhanced sparse PIC methods to improve the efficiency of the electric field computation. In section 4, the merits of the different methods are investigated thanks to two dimensional computations relating classical plasma physics test cases: the linear and non linear Landau damping as well as the diocotron instability. The conclusions are drawn in section 5, with an emphasize of the remarkable prospects of sparse grid Particle-In-Cell methods for three dimensional computations.

2. Particle-In-Cell (PIC)

2.1. **Notations.** Let us introduce some notations and functional spaces. For a multi-index $\boldsymbol{\alpha} = (\alpha_1, ..., \alpha_d) \in \mathbb{N}^d$, a function u defined on Ω an open set of $\mathbb{R}^d$, we denote by $\partial_t^{\alpha_t} u$ the partial derivative of u with respect to x_t and order α_t for $t \in \{1, ..., d\}$. Let $D^{\boldsymbol{\alpha}} u = \partial_1^{\alpha_1} ... \partial_d^{\alpha_d} u$ and consider also the notations $\partial_x^{\alpha} u := \partial_1^{\alpha} u$, $\partial_y^{\alpha} u := \partial_2^{\alpha} u$, $\partial_z^{\alpha} u := \partial_3^{\alpha} u$. We introduce the following functional spaces:

$$X_{\boldsymbol{\alpha}} := \left\{ u : \Omega \to \mathbb{R} \mid D^{\boldsymbol{\beta}} u \in C(\Omega),\ \forall \boldsymbol{\beta} \leq \boldsymbol{\alpha} \right\}, \tag{1}$$

$$X_{\boldsymbol{\alpha},0}(\kappa) := \left\{ u : \Omega \to \mathbb{R} \mid D^{\boldsymbol{\beta}} u \in C_0(\Omega),\ \|D^{\boldsymbol{\beta}} u\|_\infty \leq \kappa,\ \forall \boldsymbol{\beta} \leq \boldsymbol{\alpha} \right\} \tag{2}$$

where $\kappa \in \mathbb{R}$, $\kappa > 0$, $C(\Omega)$ denotes the space of continuous functions on Ω, $C_0(\Omega)$ denotes the space of continuous functions vanishing on the boundary and the notation $\boldsymbol{\beta} \leq \boldsymbol{\alpha}$ stands for $\beta_t \leq \alpha_t$ for all $t \in \{1, ..., d\}$. We introduce the L^p norm and supremum norm for a function $u \in L^p(\Omega)$:

$$\|u\|_p := \left(\int_\Omega |u(\mathbf{x})^p| d\mathbf{x} \right)^{1/p}, \quad \|u\|_\infty := \sup_{\mathbf{x} \in \Omega} |u(\mathbf{x})|, \tag{3}$$

and the discrete l^1 norm, l^∞ norm, minimum notation for a vector $\mathbf{u} \in \mathbb{R}^d$

$$|\mathbf{u}|_1 := \sum_{t=1}^{d} u_t, \quad |\mathbf{u}|_\infty := \max_{t \in \{1,...,d\}} u_t, \quad \min(\mathbf{u}) := \min_{t \in \{1,...,d\}} u_t. \tag{4}$$

2.2. **Standard Particle-In-Cell (STD scheme).** In this section, the non-relativistic system of Vlassov-Poisson with fixed magnetic field $\mathbf{B}$ is considered:

$$\begin{cases} \dfrac{\partial f_s}{\partial t} + \mathbf{v} \cdot \nabla_{\mathbf{x}} f_s + \dfrac{q_s}{m_s} (\mathbf{E} + \mathbf{v} \times \mathbf{B}) \cdot \nabla_{\mathbf{v}} f_s = 0, \\ \nabla \cdot \mathbf{E} = \dfrac{\rho}{\varepsilon_0}, \qquad \mathbf{E} = -\nabla \Phi, \end{cases} \tag{5}$$

In this problem, $f_s(\mathbf{x}, \mathbf{v}, t)$ is the phase-space distribution attached to the species s; q_s, m_s are the corresponding charge and mass, $\mathbf{E}$ is the electric field and ρ is the charge density obtained from the phase-space distribution of each species:

$$\rho(\mathbf{x}, t) = \sum_s \rho_s(\mathbf{x}, t) = \sum_s q_s \int f_s(\mathbf{x}, \mathbf{v}, t) d\mathbf{v}. \tag{6}$$

The standard Particle-In-Cell scheme (STD) consists of four steps repeated at each iteration in time:

(STD1) The particle distribution f_s is represented by a collection of N numerical particles. The position and velocity of the particles, denoted $(\mathbf{x}_p, \mathbf{v}_p)$, $p = 1, ..., N$, are evolved following Newton equations:

$$\frac{d\mathbf{x}_p}{dt} = \mathbf{v}_p, \qquad \frac{d\mathbf{v}_p}{dt} = \frac{q_s}{m_s}(\mathbf{E} + \mathbf{v} \times \mathbf{B})|_{\mathbf{x}=\mathbf{x}_p}. \tag{7}$$

(STD2) The charge density of each type of particle is projected onto a grid with a numerical convolution kernel, named shape function and denoted $\mathcal{S}$, and a sum over the particles (see details in the following).

(STD3) The electric field is obtained by resolving the Poisson equation from the density on the grid and differenciating the potential:

$$\Delta\Phi = -\frac{\sum_s \rho_s}{\varepsilon_0}, \quad \mathbf{E} = -\nabla\Phi \tag{8}$$

(STD4) The electric field is then evaluated at the particles positions by interpolation.

Considering a leap frog scheme and a second order finite difference scheme, the time discretization error is $\mathcal{O}(\Delta_t^2)$ and the field solver error is $\mathcal{O}(h^2)$ (see proposition 3.10), where Δ_t is the time step, h is the grid discretization corresponding to the cell size of the grid. The remaining error in the scheme results from the second step where the density is projected onto the grid.

2.3. **Projection of the density onto the grid.** The charge density of any species is approximated on a grid from a collection of numerical particles with a certain error that we shall explicit here. For ease of presentation in the following, we consider one type of particle and ommit the subscript s denoting the particle species. We consider a Monte-carlo approach to estimate the density like in [27]. Starting from the defintion, the density is recast into:

$$\rho(\mathbf{x}) = q \int f(\mathbf{x}, \mathbf{v}) d\mathbf{v} = \mathcal{Q} \int \delta(\tilde{\mathbf{x}} - \mathbf{x}) \tilde{f}(\tilde{\mathbf{x}}, \mathbf{v}) d\tilde{\mathbf{x}} d\mathbf{v}, \tag{9}$$

where $\tilde{f} = f/\mathcal{N}$ is the probability density function associated to the phase-space distribution, $\mathcal{N} = \mathcal{Q}/q$ is the total number of physical particles and $\mathcal{Q}$ is the total charge of the particles. The rewriting in equation (9) allow us to define an numerical approximation of the density in the following. We consider a grid with a discretization h (corresponding to the cell width) and, as an ersatz of the convolution kernel, a d-dimensional shape function, denoted $\mathcal{S}_d$, constructed by tensor products of one dimensional shape functions:

$$\mathcal{S}_d(\mathbf{x}) := \frac{1}{h^d} \mathcal{S}(x_1) \cdot ... \cdot \mathcal{S}(x_d), \quad \mathcal{S}(x_t) = \begin{cases} 1 - |x_t|, & \text{if } |x_t| \leq 1, \\ 0, & \text{else,} \end{cases} \tag{10}$$

$\mathcal{S}$ is generally a piecewise polynomial, named B-spline. In this paper, the shape functions $\mathcal{S}_d$ considered are B1-splines (of degree 1). Then, substituting the convolution kernel with the shape function, we define the approximation of the density with:

$$\rho_h(\mathbf{x}) := \mathcal{Q} \iint \mathcal{S}_d \left(\frac{\mathbf{x} - \tilde{\mathbf{x}}}{h} \right) \tilde{f}(\tilde{\mathbf{x}}, \mathbf{v}) d\mathbf{v} d\tilde{\mathbf{x}}. \tag{11}$$

Let $\tilde{\mathbf{X}}$ be a random variable with probability density function $\int \tilde{f}(\cdot,\mathbf{v})d\mathbf{v}$ and expected value $\mathbb{E}[\tilde{\mathbf{X}}] := \int \tilde{\mathbf{X}} dP$, where P is a probability measure. The local charge density $\mathcal{S}_d\left(\frac{\mathbf{x}-\tilde{\mathbf{X}}}{h}\right)$ being a random variable and $\boldsymbol{\xi} \mapsto \mathcal{S}_d\left(\frac{\mathbf{x}-\boldsymbol{\xi}}{h}\right)$ a mesurable function of $\mathbb{R}^n$, owing to Transfer theorem [27], we have:

$$\rho_h(\mathbf{x}) = \mathcal{Q}\iint \mathcal{S}_d\left(\frac{\mathbf{x}-\tilde{\mathbf{x}}}{h}\right)\tilde{f}(\tilde{\mathbf{x}},\mathbf{v})d\mathbf{v}d\tilde{\mathbf{x}} = \mathcal{Q}\mathbb{E}\left[\mathcal{S}_d\left(\frac{\mathbf{x}-\tilde{\mathbf{X}}}{h}\right)\right], \tag{12}$$

Since the collection of numerical particle positions $(\mathbf{x}_p)_p$ is considered as a sequence of independent realizations of the random variable $\tilde{\mathbf{X}}$, one can introduce a statistical estimator for the density based on the particle positions:

$$\rho_{h,N}(\mathbf{x}) := \frac{\mathcal{Q}}{N}\sum_{p=1}^{N}\mathcal{S}_d\left(\frac{\mathbf{x}-\mathbf{x}_p}{h}\right). \tag{13}$$

$\rho_{h,N}(\mathbf{x})$ is an estimator for the value $\rho(\mathbf{x}) = \mathcal{Q}\mathbb{E}[\delta(\mathbf{x}-\tilde{\mathbf{X}})]$ considered as a statistical quantity that can be computed as a function of the random variable $\tilde{\mathbf{X}}$. To estimate the error introduced by approximating the density on the grid with this estimator, we will evaluate the root-mean-square-error which is the classical L^2 error of the estimator as a function of $\tilde{\mathbf{X}}$.

Proposition 2.1. *Assuming enough smoothness on the probability density $\tilde{f}(\cdot,\boldsymbol{v}) \in X_{\mathbf{4}}$, the root-mean square-error is majorated by:*

$$\left(\int (\rho_{h,N}(\boldsymbol{x})-\rho(\boldsymbol{x}))^2 d\boldsymbol{x}_p\right)^{\frac{1}{2}} \leq \mathbb{V}[\rho_{h,N}(\boldsymbol{x})]^{\frac{1}{2}} + \mathrm{Bias}(\rho_{h,N}(\mathbf{x})), \tag{14}$$

where the bias and the square root variance are given by:

$$\begin{aligned}\mathrm{Bias}(\rho_{h,N})(\mathbf{x}) :&= \mathbb{E}[\rho_{h,N}(\boldsymbol{x})] - \rho_{h,N}(\boldsymbol{x}) \\ &= \underbrace{\frac{h^2}{12}\sum_{t=1}^{d}\partial_t^2\rho(\boldsymbol{x}) + \frac{h^4}{360}\sum_{t=1}^{d}\partial_t^4\rho(\boldsymbol{x})}_{\mathcal{G}_n^{\parallel}} \\ &\quad + \underbrace{\frac{h^4}{144}\sum_{\substack{t_1,t_2\in\{1,\dots,d\}\\ t_1\neq t_2}}\partial_{t_1}^2\partial_{t_2}^2\rho(\boldsymbol{x})}_{\mathcal{G}_n^{\times}} + \mathcal{O}(h^6).\end{aligned} \tag{15}$$

$$\begin{aligned}(\mathbb{V}[\rho_{h,N}](\boldsymbol{x}))^{\frac{1}{2}} :&= (\mathbb{E}[\rho_{h,N}^2(\boldsymbol{x})] - \mathbb{E}[\rho_{h,N}(\boldsymbol{x})]^2)^{\frac{1}{2}} \\ &= \underbrace{\left(\left(\frac{2}{3}\right)^d\frac{\mathcal{Q}\rho(\boldsymbol{x})}{Nh^d}\right)^{\frac{1}{2}}}_{\mathcal{P}_{n,N}} + \mathcal{O}\left(N^{-\frac{1}{2}}\right).\end{aligned} \tag{16}$$

Proof of proposition 2.1. See [27].

Remark 2.2. The root-mean-square-error is composed of two parts. First, the error stemming from the variance of the sample with a finite number of particles $\mathbb{V}[\rho_{h,N}]$, referred to as the particle sampling error and denoted $\mathcal{P}_{n,N}$ in the following. Second, the bias of the sampling $\text{Bias}(\rho_{h,N})$, the error between the expected value of the estimator and that of the the random variable $\delta(\mathbf{x}-\tilde{\mathbf{X}})$. This is a grid-based error proportional to both the mesh size and the solution smoothness with two components denoted $\mathcal{G}_n^{\parallel}$ and $\mathcal{G}_n^{\times}$ depending respectively on the non-cross and cross derivatives of the solution.

3. Merging Particle-In-Cell with sparse grids

3.1. Introduction to sparse grids.

3.1.1. *Sparse grid notations.* In this section, the sparse grid notations will be introduced for the specific framework of the so-called combination technique [20, 21]. The domain is $\Omega = [0,1]^d$, with $d \in \mathbb{N}$. We consider a sequence of anisotropic grids parametrized by an index $\mathbf{l} = (l_1, ..., l_d) \in \mathbb{N}^d$ corresponding to the level of a grid that we shall name sub-grid and denote $\Omega_{\mathbf{l}}$. The designation "sub-grid" is chosen because a sub-grid of level $\mathbf{l}$ is a subset of the Cartesian grid of level n (defined in equation (18)) for $|\mathbf{l}|_\infty \leq n$. The sub-grids are composed of the nodes:

$$\mathbf{x}_{\mathbf{l},\mathbf{j}} := (j_1 \cdot h_{l_1}, ..., j_d \cdot h_{l_d}),$$

where $h_{\mathbf{l}} := (h_{l_1}, ..., h_{l_d})$, $h_{l_t} = 2^{-l_t}$ for $t = 1, ..., d$ is the grid discretization and $\mathbf{j} \in \mathcal{J}_{\mathbf{l}}$, with

$$\begin{aligned} \mathcal{J}_{\mathbf{l}} &= \left\{ \mathbf{j} \in \mathbb{N}^d \mid j_t = 0, ..., 2^{l_t},\ t = 1, ..., d \right\}, \\ \mathcal{J}_n &= \left\{ \mathbf{j} \in \mathbb{N}^d \mid j_t = 0, ..., 2^{n},\ t = 1, ..., d \right\}, \end{aligned} \tag{17}$$

the index set of the nodes of the sub-grid of level $\mathbf{l}$ and uniform level n. Let us introduce a regular cartesian grid, which is typically the underlying grid in PIC methods or in standard interpolation, corresponding to a grid of uniform level $\mathbf{l} = (n, ..., n)$, denoted Ω_n and composed of the nodes:

$$\mathbf{x}_{n,\mathbf{j}} := (j_1 \cdot h_n, ..., j_d \cdot h_n), \tag{18}$$

where $h_n = 2^{-n}$ is the grid discretization and $\mathbf{j} \in \mathcal{J}_n$. For any grid (sub-grid or cartesian grid), we define a basis $\{\phi_{\mathbf{l},\mathbf{j}} \mid \mathbf{j} \in \mathcal{J}_{\mathbf{l}}\}$, composed by tensor products of unidimensional B-spline functions of degree m and denoted $\phi^m_{\mathbf{l},\mathbf{j}}$:

$$\phi^m_{\mathbf{l},\mathbf{j}}(\mathbf{x}) := \prod_{t=1}^{d} \phi^m_{l_t,j_t}(x_t). \tag{19}$$

The unidimensional B-spline functions are defined recursively starting from the B0-spline of degree 0 that we shall denoted $\phi^0_{l,j}$ and higher order B-splines of degree m, for $m \in \mathbb{N}^*$ defined by:

$$\phi^0_{l,j}(x) = \begin{cases} \frac{1}{h_l} & \text{if } \frac{|x - jh_l|}{h_l} \leq \frac{1}{2}, \\ 0 & \text{else}; \end{cases} \qquad \phi^m_{l,j}(x) = \frac{1}{h_l} \int_{x-\frac{h_l}{2}}^{x+\frac{h_l}{2}} \phi^{m-1}_{l,j}(\xi) d\xi. \tag{20}$$

It yiels the following definition for the B1-spline

$$\phi^1_{l,j}(x) = \begin{cases} 1 - \dfrac{|x - jh_l|}{h_l} & \text{if } \dfrac{|x - jh_l|}{h_l} \leq 1, \\ 0 & \text{else.} \end{cases} \tag{21}$$

Proposition 3.1. *The B-spline functions verify the following properties:*

$$\prod_{t=1}^{d}\frac{1}{h_{l_t}}\int \phi^m_{l,j}(\boldsymbol{x})d\boldsymbol{x}=1 \text{ (Unit mean)}, \quad \sum_{j\in\mathcal{J}_l}\phi^m_{l,j}(\boldsymbol{x})=1 \text{(Partition of unit)},$$
$$\phi^m_{l,j}(\boldsymbol{x}_{l,j}-\boldsymbol{x})=\phi^m_{l,j}(\boldsymbol{x}_{l,j}+\boldsymbol{x}) \text{(Parity)}.$$

Proof of proposition 3.1. It follows from the definition. □

3.1.2. *Combination technique.* The so-called combination technique [20, 21] is a method of interpolation using evaluations of the function on the nodes of sub-grids. The interpolant is obtained by a linear combination of partial representations of the function on the sub-grids. Considering the sub-grids $\Omega_{\mathbf{l}}$ with $\mathbf{l}\in\mathcal{L}(n,\sigma)$, where

$$\mathcal{L}(n,\sigma):=\{\mathbf{l}\in\mathbb{N}^d \mid |\mathbf{l}|_1=n+d-1-\sigma,\ \mathbf{l}\geq(1,...,1)\}, \tag{22}$$

is the level set of the sub-grids considered in the combination for $\sigma=0,...,d-1$, the degree m interpolant of the function on each sub-grid, denoted $f^m_{\mathbf{l}}$, is defined as:

$$f^m_{\mathbf{l}}(\mathbf{x}):=\sum_{\mathbf{j}\in\mathcal{J}_{\mathbf{l}}}\alpha_{\mathbf{l},\mathbf{j}}\phi^m_{\mathbf{l},\mathbf{j}}(\mathbf{x}), \tag{23}$$

where the coefficients $\alpha_{\mathbf{l},\mathbf{j}}$ are determined by the resolution of a linear system with unknowns $(\alpha_{\mathbf{l},\mathbf{j}})_{\mathbf{j}\in\mathcal{J}_{\mathbf{l}}}$ to meet the interpolation conditions on the sub-grid nodes:

$$\forall\mathbf{j}\in\mathcal{J}_{\mathbf{l}},\quad f^m_{\mathbf{l}}(\mathbf{x}_{\mathbf{l},\mathbf{j}})=\sum_{\tilde{\mathbf{j}}\in\mathcal{J}_{\mathbf{l}}}\alpha_{\mathbf{l},\tilde{\mathbf{j}}}\phi^m_{\mathbf{l},\tilde{\mathbf{j}}}(\mathbf{x}_{\mathbf{l},\mathbf{j}})=f(\mathbf{x}_{\mathbf{l},\mathbf{j}}) \tag{24}$$

The sparse grid interpolant, denoted f^m_n, is then defined on the entire domain as:

$$f^m_n(\mathbf{x}):=\sum_{\sigma=0}^{d-1}(-1)^\sigma\binom{d-1}{\sigma}\sum_{\mathbf{l}\in\mathcal{L}(n,\sigma)}f^m_{\mathbf{l}}(\mathbf{x}), \tag{25}$$

where $\binom{d-1}{\sigma}:=\dfrac{(d-1)!}{\sigma!(d-1-\sigma)!}$ is the notation for the binomial coefficient.

Proposition 3.2. *Let f be a smooth function with a pointwise error expression of the form:*

$$f(\boldsymbol{x})-f^m_l(\boldsymbol{x})=\sum_{m=1}^{d}\sum_{\{1,...,m\}\subset\{1,...,d\}}\tau_{1,...,m}(\boldsymbol{x};h_{l_1},...,h_{l_m})h^2_{l_1}...h^2_{l_m}, \tag{26}$$

with bounded $\|\tau_{1,...,m}(\cdot;h_{l_1},...,h_{l_m})\|_\infty\leq\kappa$, $\kappa\in\mathbb{R}$, $\kappa>0$. The sparse grid interpolant of the function converges to the exact solution in L^p norm when the grid discretization tends towards zero:

$$\|f^m_n-f\|_p=\mathcal{O}(log_2(h_n^{-1})^{d-1}h^2_n),\qquad 1\leq p\leq\infty, \tag{27}$$

Proof of proposition 3.2. See [20].

The combination technique is motivated by the reduction of the number of interpolation nodes (from $\mathcal{O}(h_n^{-d})$ to $\mathcal{O}(\log_2(h_n^{-1})^{d-1}h_n^{-1})$) while achieving nearly the same precision ($\mathcal{O}(\log_2(h_n^{-1})^{d-1}h_n^2)$) than the standard interpolation ($\mathcal{O}(h_n^2)$).

Remark 3.3. Assuming that $\forall\mathbf{x}\in\Omega$, $f(\mathbf{x})\geq 0$, the sparse grid interpolant f^m_n is not nonnegative in the general case.

3.2. **Application to Particle-In-Cell discretizations.** In this section, two applications of the combination technique to Particle-In-Cell methods are presented. In the regular PIC approximation, the main drawback is the statistical error decreasing with the number of particles per cell. Indeed, the particle sampling and the grid based errors scale respectively as $\mathcal{O}(1/\sqrt{Nh_n^d})$ and $\mathcal{O}(h_n^2)$, h_n being the mesh size of the Cartesian grid defined by equation (18) and N the total number of particles. These two error estimates together lead to the following onerous conditions of convergence of the scheme $h_n^2 \ll 1$, $Nh_n^d \gg 1$ which can require an extremely large number of particles, specifically for three dimensional simulations. The combination technique achieves a representation of a function using a sequence of sparse grids coarser than the standard Cartesian mesh. This ends up in a reduced number of interpolation nodes and, accordingly an increased mean number of particle per cell. This feature motivates the application of sparse grid techniques to PIC methods.

Let us introduce the hierarchical shape function of level $\mathbf{l} = (l_1, ..., l_d)$ constructed by tensor products of the unidimensional shape functions introduced in equation (10):

$$\mathcal{S}_{d,\mathbf{l}}(\mathbf{x}) := \prod_{t=1}^{d} \frac{1}{h_{l_t}} \mathcal{S}\left(\frac{x_t}{h_{l_t}}\right), \tag{28}$$

with support, magnitude depending on the discretization of the sub-grid $\Omega_{\mathbf{l}}$ (see figure 1) and whose role is to approximate the convolution kernel $\delta(\mathbf{x})$ on this sub-grid. From this, recalling section 2.3, one is then able to define a hierarchical estimator for the density at each node of the sub-grid $\Omega_{\mathbf{l}}$ and denoted $\rho_{\mathbf{l},\mathbf{j},N}$:

$$\forall \mathbf{j} \in \mathcal{J}_{\mathbf{l}}, \qquad \rho_{\mathbf{l},\mathbf{j},N} = \frac{\mathcal{Q}}{N} \sum_{p=1}^{N} \mathcal{S}_{d,\mathbf{l}}(\mathbf{x}_{\mathbf{l},\mathbf{j}} - \mathbf{x}_p), \tag{29}$$

This estimator corresponds to the projection of the density onto the sub-grid. The error between the hierarchical estimator and the density can be estimated by the bias and the square root variance of the estimator. Recalling proposition 2.1:

$$\text{Bias}(\rho_{\mathbf{l},\mathbf{j},N}) = \sum_{m=1}^{d} \sum_{\{1,...,m\} \subset \{1,...,d\}} \tau_{1,...,m}(\mathbf{x}_{\mathbf{l},\mathbf{j}}\,; h_{l_1}, ..., h_{l_m}) h_{l_1}^2 ... h_{l_m}^2, \tag{30}$$

$$(\mathbb{V}[\rho_{\mathbf{l},\mathbf{j},N}])^{\frac{1}{2}} = \zeta_{1,...,d}(\mathbf{x}_{\mathbf{l},\mathbf{j}}\,; h_{l_1}, ..., h_{l_d})(Nh_{l_1} ... h_{l_d})^{-\frac{1}{2}}, \tag{31}$$

where

$$\tau_{1,...,m}(\cdot; h_{l_1}, ..., h_{l_m}) = \left(\frac{1}{12}\right)^m \partial_1^2 ... \partial_m^2 \rho + \mathcal{O}(h_{l_1}^2, ..., h_{l_m}^2), \tag{32}$$

$$\zeta_{1,...,d}(\cdot; h_{l_1}, ..., h_{l_d}) = \left(\left(\frac{2}{3}\right)^d \mathcal{Q}\rho\right)^{\frac{1}{2}} + \mathcal{O}\left(N^{-\frac{1}{2}}\right). \tag{33}$$

The dependances of $h_{l_1}, ..., h_{l_m}, h_{l_1}, ..., h_{l_d}$ for the functions $\tau_{1,...,m}$, $\zeta_{1,...,d}$ mean that the functions are evaluated at the nodes of a grid with discretization $h_{\mathbf{l}}$.

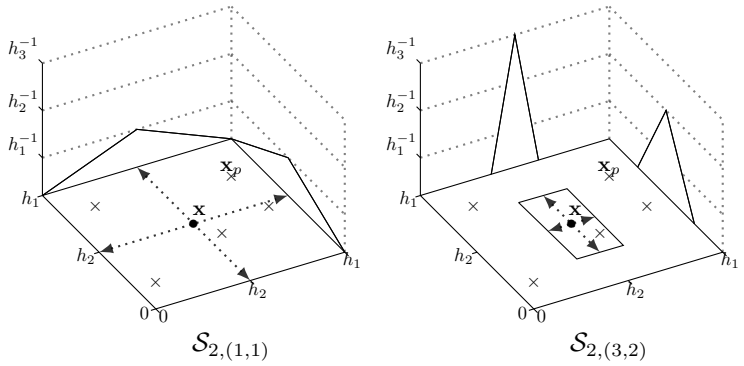

Figure 1. Examples of hierarchical shape function $\mathcal{S}_{d,\mathbf{l}}(\mathbf{x}-\mathbf{x}_p)$ in the two dimensional case.

Lemma 3.4. *Let f be a smooth function with a pointwise error expression of the form:*

$$f(\boldsymbol{x}) - f_{\boldsymbol{l}}^m(\boldsymbol{x}) = \zeta_{1,\dots,d}(\boldsymbol{x}; h_{l_1}, \dots, h_{l_d})(Nh_{l_1}\dots h_{l_d})^{-\frac{1}{2}} \tag{34}$$

with bounded $\|\zeta_{1,\dots,d}(\cdot; h_{l_1}, \dots, h_{l_d})\|_\infty \leq \kappa$. The sparse grid interpolant of the function converges to the exact solution in L^p norm with:

$$\|f_n^m - f\|_p = \mathcal{O}(log_2(h_n^{-1})^{d-1}(Nh_n)^{-\frac{1}{2}}), \qquad 1 \leq p \leq \infty. \tag{35}$$

Proof of lemma 3.4. The proof is given in appendix A.

Remark 3.5. The bias of the hierarchical estimator on a sub-grid verifies the assumption of equation (26) and the square root variance verifies the assumption of equation (34). Therefore, an ingenious combination of these projections of the density (see details in the following sections) shall lead to cancellations and an error scaling with $\mathcal{O}(\log_2(h_n^{-1})^{d-1}(h_n^2 + (Nh_n)^{-\frac{1}{2}}))$. This feature, resulting from the tensor product form of the shape function $\mathcal{S}$, is the motivation for the application of sparse grid combination to PIC.

3.2.1. *Discretization on hybrid grids (HG scheme).* In this section, a first sparse grid application to PIC methods [2], is presented. In order to take advantage of the cancellations exposed in the precedent section, a sparse grid interpolant of the density is constructed. The density is projected onto each sub-grid, achieving a reduction of the statistical error thanks to the large cells of the sub-grids, then evaluated onto the Cartesian grid with the combination technique. Let us introduce the corresponding scheme, that we shall name the Hybrid Grid Particle-In-Cell (HG) scheme (owing to the Cartesian grid and sub-grids considered within the scheme):

(HG1) Similar to (STD1)

(HG2) On each sub-grid, the hierarchical estimator defined in equation (29) provides a partial representation of the density; and, using the combination technique we define a sparse grid interpolant of the density on the entire

domain with basis functions defined in equation (19), denoted $\rho^m_{n,N}$:

$$\rho^m_{n,N}(\mathbf{x}) = \sum_{\sigma=0}^{d-1}(-1)^\sigma \binom{d-1}{\sigma} \sum_{\mathbf{l}\in\mathcal{L}(n,\sigma)} \underbrace{\sum_{\mathbf{j}\in\mathcal{J}_\mathbf{l}} \alpha_{\mathbf{l},\mathbf{j}}\phi^m_{\mathbf{l},\mathbf{j}}(\mathbf{x})}_{=\rho^m_\mathbf{l}(\mathbf{x})}, \tag{36}$$

where $\rho^m_\mathbf{l}$ is the sparse grid interpolant of the density on the sub-grid, $\mathcal{L}(n,\sigma)$, $\mathcal{J}_\mathbf{l}$ are defined in equation (22), (17) and the coefficients $\alpha_{\mathbf{l},\mathbf{j}}$ are determined by the interpolation conditions in equations (24).

(HG3) On the Cartesian grid, an approximation of the electric field, denoted $\mathbf{E}_{n,\mathbf{j}}$, is obtained by resolving the Poisson equation from the sparse grid interpolant of the density and differenciating the potential with a finite difference scheme:

$$\forall \mathbf{j}\in\mathcal{J}_n, \quad \mathbf{E}_{n,\mathbf{j}} = -\nabla_{h_n}\Phi_{n,\mathbf{j}}, \quad \Delta_{h_n}\Phi_{n,\mathbf{j}} = -\frac{\rho^m_{n,N}(\mathbf{x}_{n,\mathbf{j}})}{\varepsilon_0}, \tag{37}$$

where ∇_{h_n} and Δ_{h_n} are the second order discrete finite difference operators defined on the Cartesian grid by:

$$\Delta_{h_n}\Phi_{\mathbf{l},\mathbf{j}} := \sum_{t=1}^{d}(\delta^+_{t,h_n}\delta^-_{t,h_n})\Phi_{n,\mathbf{j}}, \quad \nabla_{h_n}\Phi_{n,\mathbf{j}} := \left(\delta^0_{t,h_n}\Phi_{n,\mathbf{j}}\right)_{t=1,\dots,d}, \tag{38}$$

$\delta^-_{t,h_{l_t}}$, $\delta^+_{t,h_{l_t}}$ are left-sided, right-sided differences and $\delta^0_{t,h_{l_t}}$ is centered difference:

$$\delta^+_{t,h_{l_t}}\Phi_{\mathbf{l},\mathbf{j}} := \frac{\Phi_{\mathbf{l},\mathbf{j}+\mathbf{i}_t} - \Phi_{\mathbf{l},\mathbf{j}}}{h_{l_t}}, \quad \delta^-_{t,h_{l_t}}\Phi_{\mathbf{l},\mathbf{j}} := \frac{\Phi_{\mathbf{l},\mathbf{j}} - \Phi_{\mathbf{l},\mathbf{j}-\mathbf{i}_t}}{h_{l_t}}, \tag{39}$$

$$\delta^0_{t,h_{l_t}}\Phi_{\mathbf{l},\mathbf{j}} := \frac{\Phi_{\mathbf{l},\mathbf{j}+\mathbf{i}_t} - \Phi_{\mathbf{l},\mathbf{j}-\mathbf{i}_t}}{2h_{l_t}}, \tag{40}$$

and $\mathbf{i}_t \in \mathbb{N}^d$ is the index whose value is 1 along the t^{th} coordinate and 0 elsewhere.

(HG4) The electric field is evaluated at particle positions with standard interpolation on the Cartesian grid:

$$\mathbf{E}^m_n(\mathbf{x}_p) := \sum_{\mathbf{j}\in\mathcal{J}_n} \alpha_{n,\mathbf{j}}\phi^m_{\mathbf{n},\mathbf{j}}(\mathbf{x}_p), \tag{41}$$

where coefficients $\alpha_{n,\mathbf{j}}$ are determined by the following interpolation conditions:

$$\forall \mathbf{j}\in\mathcal{J}_n, \quad \mathbf{E}^m_n(\mathbf{x}_{n,\mathbf{j}}) = \sum_{\tilde{\mathbf{j}}\in\mathcal{J}_n} \alpha_{n,\tilde{\mathbf{j}}}\phi^m_{n,\tilde{\mathbf{j}}}(\mathbf{x}_{n,\mathbf{j}}) = \mathbf{E}_{n,\mathbf{j}}. \tag{42}$$

and $\mathbf{E}_{n,\mathbf{j}}$ is defined by equation (37).

Proposition 3.6. *The sparse grid interpolant conserves the total charge:*

$$\int \rho^m_{n,N}(\boldsymbol{x})d\boldsymbol{x} = \int \rho(\boldsymbol{x})d\boldsymbol{x} = \mathcal{Q}. \tag{43}$$

Remark 3.7. The positivity of the charge density is not preserved by the sparse grid interpolation (see remark 3.3).

Proposition 3.8. *Assuming $\rho \in X_{\mathbf{2}}(\kappa)$, the sparse grid interpolant of the density converges to the exact solution in L^p norm, $1 \leq p \leq \infty$ when the grid discretization tends towards zero and the mean number of particles per cell tends towards $+\infty$:*

$$\|\rho_{n,N}^m - \rho\|_p = \mathcal{O}\left(\underbrace{h_n^2}_{\mathcal{G}_n^{\parallel}} + \underbrace{log_2(h_n^{-1})^{d-1} h_n^2}_{\mathcal{G}_n^{\times}} + \underbrace{log_2(h_n^{-1})^{d-1}(Nh_n)^{-\frac{1}{2}}}_{\mathcal{P}_{n,N}} \right). \tag{44}$$

For two dimensional computations carried out with B1-splines, the following estimation holds true for the sparse grid interpolants of the density:

$$\begin{aligned} \|\rho_{n,N}^m - \rho\|_p \leq & \left(\frac{5}{24}(\|\partial_x^2 \rho\|_\infty + \|\partial_y^2 \rho\|_\infty) + \frac{13}{576}\left(\frac{5}{4}n - 1\right)\|\partial_x^2 \partial_y^2 \rho\|_\infty \right) h_n^2 \\ & + \frac{2}{3}((\sqrt{2}+1)n - 1)\left(\frac{\mathcal{Q}\|\rho\|_\infty}{Nh_n}\right)^{\frac{1}{2}}. \end{aligned} \tag{45}$$

Remark 3.9. The benefit of the combination technique as a noise reduction strategy is pointed out by the equation (44). Owing to the projection of the density onto the sub-grids, the particle sampling error is reduced from $\mathcal{O}((Nh_n^d)^{-1/2})$ to $\mathcal{O}(\log_2(h_n^{-1})^{d-1}(Nh_n)^{-1/2})$. The profit is significant for refined grids as well as three dimensional problems. Conversely, an increase of the grid-based error results from the combination; the grid-based error is increased from $\mathcal{O}(h_n^2)$ to $\mathcal{O}(\log_2(h_n^{-1})^{d-1}h_n^2)$. Though $h_n^2 \approx \log_2(h_n^{-1})^{d-1}h_n^2$, the loss may appears negligible, however the dominant component of the error becomes $\mathcal{G}_n^{\times}$ (with dependences on $2d^{\text{th}}$ order derivatives). As a comparison, the grid-based error of regular PIC methods is dominated by the $\mathcal{G}_n^{\parallel}$ component (with dependences on 2^{nd} order derivatives). This feature indicates a drawback of the combination technique and may limit the efficiency of the method when the solution develops strong gradients not aligned with the Cartesian grid.

Proposition 3.10. *Assuming enough smoothness on ρ so that $\Phi \in X_{\mathbf{5},0}(\gamma)$, $\rho \in X_{\mathbf{3}}(\kappa)$, the sparse grid interpolant of the electric field converges to the exact solution in L^p norm, $1 \leq p \leq \infty$ when the grid discretization tends towards zero and the number of particles tends towards $+\infty$:*

$$\|\boldsymbol{E}_n^m - \boldsymbol{E}\|_p = \mathcal{O}\left(\underbrace{h_n^2}_{\mathcal{G}_n^{\parallel}} + \underbrace{log_2(h_n^{-1})^{d-1} h_n^2}_{\mathcal{G}_n^{\times}} + \underbrace{log_2(h_n^{-1})^{d-1}(Nh_n)^{-\frac{1}{2}}}_{\mathcal{P}_{n,N}} \right), \tag{46}$$

where $\boldsymbol{E} = -\nabla\Phi$, $\Delta\Phi = -\rho/\varepsilon_0$. For two dimensional computations carried out with B1-splines, the following estimations hold true for the sparse grid interpolants

of the electric field:

$$
\begin{aligned}
(47)\quad \|\boldsymbol{E}_n^m - \boldsymbol{E}\|_p \leq \Bigg(& \frac{5}{24}\|\boldsymbol{\Delta}_{h_n}^{-1}\|_\infty(\|\nabla\partial_x^2\rho\|_\infty + \|\nabla\partial_y^2\rho\|_\infty + \|\nabla\partial_x^4\Phi\|_\infty \\
& + \|\nabla\partial_y^4\Phi\|_\infty) + \frac{1}{3}\begin{pmatrix} \|\partial_x^3\Phi\|_\infty \\ \|\partial_y^3\Phi\|_\infty \end{pmatrix} + \frac{1}{8}\left(\|\nabla\partial_x^2\Phi\|_\infty + \|\nabla\partial_y^2\Phi\|_\infty\right) \\
& + \frac{13}{576}\left(\frac{5}{4}n - 1\right)\|\boldsymbol{\Delta}_{h_n}^{-1}\|_\infty\left(\|\nabla\partial_x^2\partial_y^2\rho\|_\infty\right)\Bigg) h_n^2 \\
& + \frac{2}{3}((\sqrt{2}+1)n - 1)\|\boldsymbol{\Delta}_{h_n}^{-1}\|_\infty\left(\frac{\mathcal{Q}}{Nh_n}\right)^{\frac{1}{2}}\|\nabla\rho\|_\infty^{\frac{1}{2}},
\end{aligned}
$$

where $\boldsymbol{\Delta}_{h_n}^{-1}$ *is the inverse matrix of the Laplacian problem.*

Proof of proposition 3.6.

$$
\begin{aligned}
\int \rho_{n,N}^m(\mathbf{x})d\mathbf{x} &= \int \sum_{\sigma=0}^{1}(-1)^\sigma \sum_{\mathbf{l}\in\mathcal{L}(n,\sigma)}\sum_{\mathbf{j}\in\mathcal{J}_\mathbf{l}}\frac{\mathcal{Q}}{N}\sum_{p=1}^{N}\mathcal{S}_{d,\mathbf{l}}(\mathbf{x}_{\mathbf{l},\mathbf{j}} - \mathbf{x}_p)\phi_{\mathbf{l},\mathbf{j}}^m(\mathbf{x})d\mathbf{x} \\
&= \sum_{\sigma=0}^{1}(-1)^\sigma \sum_{\mathbf{l}\in\mathcal{L}(n,\sigma)}\frac{\mathcal{Q}}{N}\sum_{p=1}^{N}\underbrace{\sum_{\mathbf{j}\in\mathcal{J}_\mathbf{l}}\mathcal{S}_{d,\mathbf{l}}(\mathbf{x}_{\mathbf{l},\mathbf{j}} - \mathbf{x}_p)}_{=\prod_{t=1}^{d}h_{l_t}^{-1}}\underbrace{\int\phi_{\mathbf{l},\mathbf{j}}^m(\mathbf{x})d\mathbf{x}}_{=\prod_{t=1}^{d}h_{l_t}} \\
&= \underbrace{\sum_{\mathbf{l}\in\mathcal{L}(n,0)}\mathcal{Q}}_{\text{n terms}} - \underbrace{\sum_{\mathbf{l}\in\mathcal{L}(n,1)}\mathcal{Q}}_{\text{n-1 terms}} \\
&= \mathcal{Q}.\ \square
\end{aligned}
$$

Proof of proposition 3.8. The proof is given with B1-splines (i.e $m = 1$ in the following). Let $\mathbf{l} = (l_1, l_2)$ be a level such that $\mathbf{l} \in \mathcal{L}(n,\sigma)$ for $\sigma = 0, 1$. Owing to the partition of unit property of the basis functions, the local error between the density and its partial representation on the sub-grid $\Omega_\mathbf{l}$ is recast into:

$$
(48)\qquad \rho_\mathbf{l}^m(\mathbf{x}) - \rho(\mathbf{x}) = \sum_{\mathbf{j}\in\mathcal{J}_\mathbf{l}}(\rho_{\mathbf{l},\mathbf{j},N} - \rho(\mathbf{x}_{\mathbf{l},\mathbf{j}}) + \rho(\mathbf{x}_{\mathbf{l},\mathbf{j}}) - \rho(\mathbf{x}))\phi_{\mathbf{l},\mathbf{j}}^m(\mathbf{x}).
$$

Let $\mathbf{x}_{\mathbf{l},\mathbf{j}} - \mathbf{x} = (\delta_1, \delta_2)^T$. Assuming $\rho \in X_{\mathbf{4}}$, a Taylor expansion of the density at the sub-grid nodes in x-direction and y-direction gives us:

$$
\begin{aligned}
(49)\qquad \rho(\mathbf{x}_{\mathbf{l},\mathbf{j}}) - \rho(\mathbf{x}) = {} & \partial_x\rho(\mathbf{x})\delta_1 + \partial_y\rho(\mathbf{x})\delta_2 + \frac{1}{2}(\partial_x^2\rho(\mathbf{x})\delta_1^2 + \partial_y^2\rho(\mathbf{x})\delta_2^2 \\
& + 2\partial_x\partial_y\rho(\mathbf{x})\delta_1\delta_2) + \frac{1}{6}(\partial_x^3\rho(\mathbf{x})\delta_1^3 + 3\partial_x^2\partial_y\rho(\mathbf{x})\delta_1^2\delta_2 \\
& + 3\partial_x\partial_y^2\rho(\mathbf{x})\delta_1\delta_2^2 + \partial_y^3\rho(\mathbf{x})\delta_2^3) + \frac{1}{24}(\partial_x^4\rho(\mathbf{x})\delta_1^4 \\
& + 4\partial_x^3\partial_y\rho(\mathbf{x})\delta_1^3\delta_2 + 6\partial_x^2\partial_y^2\rho(\mathbf{x})\delta_1^2\delta_2^2 + \partial_y^4\rho(\mathbf{x})\delta_2^4).
\end{aligned}
$$

Owing to the support of the degree B1-splines, for the orders $p_1, p_2 \in \mathbb{N}$:

$$
(50)\quad \delta_1^{p_1}\delta_2^{p_2}\phi_{\mathbf{l},\mathbf{j}}^m(\mathbf{x}) = \begin{cases} \dfrac{\delta_1^{p_1}\delta_2^{p_2}}{h_{l_1}h_{l_2}}(h_{l_1} - |\delta_1|)(h_{l_2} - |\delta_2|) & \text{if } |\delta_1| < h_{l_1}, |\delta_2| < h_{l_2}, \\ 0 & \text{else.} \end{cases}
$$

Introducing the notation for $t = 1, 2$:

$$\delta_t^\star := \begin{cases} \delta_t & \text{if } \delta_t > 0, \\ h_{l_t} + \delta_t & \text{if } \delta_t < 0, \end{cases} \tag{51}$$

where $0 \leq \delta_t^\star \leq h_{l_t}$, we deduce from equation (50):

$$\sum_{\mathbf{j}\in\mathcal{J}_\mathbf{l}} \delta_1^{p_1}\delta_2^{p_2}\phi_{\mathbf{l},\mathbf{j}}^m(\mathbf{x}) = \begin{cases} \delta_1^\star(h_{l_1} - \delta_1^\star) & \text{if } (p_1,p_2) = (2,0), \\ \delta_2^\star(h_{l_2} - \delta_2^\star) & \text{if } (p_1,p_2) = (0,2), \\ \delta_1^\star\delta_2^\star(h_{l_1} - \delta_1^\star)(h_{l_2} - \delta_2^\star) & \text{if } (p_1,p_2) = (2,2), \\ 0 & \text{if } p_1 = 1 \text{ or } p_2 = 1. \end{cases} \tag{52}$$

Note that the quantity $\delta_t^\star(h_{l_t} - \delta_t^\star)$ implicitly depends on the grid discretization $h_{l_t}^2$ and is actually upper bounded by $h_{l_t}^2/4$). Let us introduce the interpolation error functions ξ_1, ξ_2, $\xi_{1,2}$ such that:

$$\begin{aligned} &h_{l_1}^2\xi_1(\mathbf{x};h_{l_1}) = \frac{1}{2}\delta_1^\star(h_{l_1} - \delta_1^\star)\partial_x^2\rho(\mathbf{x}), \quad h_{l_2}^2\xi_2(\mathbf{x};h_{l_2}) = \frac{1}{2}\delta_2^\star(h_{l_2} - \delta_2^\star)\partial_y^2\rho(\mathbf{x}), \\ &h_{l_1}^2h_{l_2}^2\xi_{1,2}(\mathbf{x};h_{l_1},h_{l_2}) = \frac{1}{4}\delta_1^\star\delta_2^\star(h_{l_1} - \delta_1^\star)(h_{l_2} - \delta_2^\star)\partial_x^2\partial_y^2\rho(\mathbf{x})\,. \end{aligned} \tag{53}$$

From this, with the bias, variance expressions, stated in equations (30),(31), and owing to the partition of unit property of basis functions:

$$\begin{aligned} \rho_\mathbf{l}^m(\mathbf{x}) - \rho(\mathbf{x}) = &(\tilde{\tau}_1(\mathbf{x};h_{l_1}) + \xi_1(\mathbf{x};h_{l_1}))h_{l_1}^2 + (\tilde{\tau}_2(\mathbf{x};h_{l_2}) + \xi_2(\mathbf{x};h_{l_2}))h_{l_2}^2 \\ &+ (\tilde{\tau}_{1,2}(\mathbf{x};h_{l_1},h_{l_2}) + \xi_{1,2}(\mathbf{x};h_{l_1},h_{l_2}))h_{l_1}^2h_2^2 \\ &+ \tilde{\zeta}_{1,2}(\mathbf{x};h_1,h_2)(Nh_{l_1}h_{l_2})^{-\frac{1}{2}}, \end{aligned} \tag{54}$$

where for a function $\omega_{1,\dots,m}$ the notation $\tilde{\omega}_{1,\dots,m}$ stands for:

$$\tilde{\omega}_{1,\dots,m}(\mathbf{x};h_{l_1},\dots,h_{l_m}) := \sum_{\mathbf{j}\in\mathcal{J}_\mathbf{l}} \omega_{1,\dots,m}(\mathbf{x}_{\mathbf{l},\mathbf{j}};h_{l_1},\dots,h_{l_m})\phi_{\mathbf{l},\mathbf{j}}^m(\mathbf{x}), \tag{55}$$

and the functions $\tau_1, \tau_2, \tau_{1,2}, \zeta_{1,2}$ are explicited in equations (32-33). Assuming $\rho \in X_\mathbf{2}(\kappa)$, the coefficients are bounded by $\|\xi_t(\cdot;h_{l_t})\|_\infty \leq \kappa/8$, $\|\tilde{\tau}_t(\cdot;h_{l_t})\|_\infty \leq \kappa/12$, for $t = 1, 2$, $\|\xi_{1,2}(\cdot;h_{l_1},h_{l_2})\|_\infty \leq \kappa/64$, $\|\tilde{\tau}_{1,2}(\cdot;h_{l_1},h_{l_2})\|_\infty \leq \kappa/144$, $\|\tilde{\zeta}_{1,2}(\cdot;h_{l_1},h_{l_2})\|_\infty \leq (4\mathcal{Q}\kappa/9)^{\frac{1}{2}}$ and using proposition 3.2, lemma 3.4:

$$\|\rho_{n,N}^m - \rho\|_p \leq \kappa\left(\frac{5}{12} + \frac{13}{576}\left(\frac{5}{4}n - 1\right)\right)h_n^2 + \frac{2}{3}((\sqrt{2}+1)n - 1)\left(\frac{\kappa\mathcal{Q}}{Nh_n}\right)^{\frac{1}{2}}.\square \tag{56}$$

Idea of the proof of proposition 3.10. Only the guidelines of the proof are provided, the details being specified for that of proposition 3.11. Let the Poisson problem with the truncation error $(h_n^2\boldsymbol{\sigma}^{(\Delta)})$ of the discrete laplacian in matrix notation:

$$\boldsymbol{\Delta}_{h_n}\boldsymbol{\Phi} = -\boldsymbol{\rho} + h_n^2\boldsymbol{\sigma}^{(\Delta)} + \mathcal{O}(h_n^3), \tag{57}$$

Introducing the sparse grid interpolant of the density and using invertibility of the matrix $\boldsymbol{\Delta}_{h_n}$, one gets:

$$\boldsymbol{\Phi} - \underbrace{(-\boldsymbol{\Delta}_{h_n}^{-1}\boldsymbol{\rho}_{n,N}^m)}_{=\boldsymbol{\Phi}_{n,\mathbf{j}}} = \boldsymbol{\Delta}_{h_n}^{-1}\left(\boldsymbol{\rho}_{n,N}^m - \boldsymbol{\rho} + h_n^2\boldsymbol{\sigma}^{(\Delta)} + \mathcal{O}(h_n^3)\right). \tag{58}$$

Applying $\boldsymbol{\nabla}_{h_n}$ to equation (58), owing to linearity and because the operators $\boldsymbol{\nabla}_{h_n}$ and $\boldsymbol{\Delta}_{h_n}^{-1}$ commutate (since $\boldsymbol{\nabla}_{h_n}$ and $\boldsymbol{\Delta}_{h_n}$ do), and introducing the following truncation error of the discrete gradient:

$$\nabla\boldsymbol{\Phi} - \nabla_{h_n}\boldsymbol{\Phi} = h_n^2\boldsymbol{\sigma}^{(\nabla)} + \mathcal{O}(h_n^4). \tag{59}$$

one gets, summing equation (59) to (58):

$$\underbrace{\nabla\boldsymbol{\Phi} - \nabla_{h_n}\boldsymbol{\Phi}_{n,\mathbf{j}}}_{=\mathbf{E}_{n,\mathbf{j}}-\mathbf{E}(\mathbf{x}_{n,\mathbf{j}})} = \underbrace{\boldsymbol{\Delta}_{h_n}^{-1}}_{(\star)}\left(\underbrace{\nabla_{h_n}(\boldsymbol{\rho}_{n,N}^m - \boldsymbol{\rho})}_{(\star\star)} + h_n^2\underbrace{\nabla_{h_n}\boldsymbol{\sigma}^{(\Delta)}}_{(\star\star\star)} + \underbrace{\nabla_{h_n}\mathcal{O}(h_n^3)}_{(\star\star\star)}\right) + h_n^2\boldsymbol{\sigma}^{(\nabla)} + \mathcal{O}(h_n^4). \tag{60}$$

- $(\star)$ $\boldsymbol{\Delta}_{h_n}^{-1}$ is uniformely bounded by a constant independent of the grid driscretization h_n (the maximum eigenvalue is bounded).
- $(\star\star)$ Using a Taylor expansion, this term scales with $\nabla(\rho_{n,N}^m - \rho)$. Retaking arguments of proof 3.8, the latter scales as equation (44).
- $(\star\star\star)$ Using a Taylor expansion, the terms scales with $\nabla\boldsymbol{\sigma}^{(\Delta)}$ and $\mathcal{O}(h_n^3)$.

Eventually, an interpolation is added for the term $\mathbf{E}(\mathbf{x}_{n,\mathbf{j}}) - \mathbf{E}(\mathbf{x})$ (see proof of proposition 3.11). □

3.2.2. *Discretization on sub-grids (SG scheme).* In this section, a second application of the combination technique to PIC methods [1] is presented. This implementation does not use a projection of the density onto the Cartesian grid. The idea is to deposit the charge density, solve the Poisson equation, differentiate the electric potential on each sub-grid and eventually interpolate the electric field from the sub-grids at particle positions by means of the combination technique. Solving the Poisson problem on each sub-grid rather than on the Cartesian grid, is likely to speed-up the computations. Indeed, the gain may be coarsely estimated by the reduced number of cells in all the sub-grids $\mathcal{O}(\log_2(h_n^{-1})^{d-1}h_n^{-1})$ compared to the Cartesian mesh ($\mathcal{O}(h_n^{-d})$). Let us introduce the scheme, that we shall name the Sub-Grid Particle-In-Cell (SG) scheme in the following:

- (SG1) Similar to (STD1).
- (SG2) The density is projected onto each sub-grid with the hierarchical estimator, defined in equation (29), in order to get a partial representation of the density on the sub-grid nodes.
- (SG3) An approximation of the electric field on each sub-grid, denoted $\mathbf{E}_{\mathbf{l},\mathbf{j}}$, is obtained by resolving the Poisson equation from the partial representation of the density on the corresponding sub-grid and differentiating the potential with a finite difference scheme:

$$\mathbf{E}_{\mathbf{l},\mathbf{j}} = -\nabla_{h_\mathbf{l}}\Phi_{\mathbf{l},\mathbf{j}}, \quad \Delta_{h_\mathbf{l}}\Phi_{\mathbf{l},\mathbf{j}} = -\frac{\rho_{\mathbf{l},\mathbf{j},N}}{\varepsilon_0}, \tag{61}$$

where $\nabla_{h_\mathbf{l}}$ and $\Delta_{h_\mathbf{l}}$ are the discrete second order finite difference operators defined on the sub-grid $\Omega_\mathbf{l}$ by:

$$\Delta_{h_\mathbf{l}}\Phi_{\mathbf{l},\mathbf{j}} := \sum_{t=1}^{d}(\delta_{t,h_{l_t}}^{+}\delta_{t,h_{l_t}}^{-})\Phi_{\mathbf{l},\mathbf{j}}, \quad \nabla_{h_\mathbf{l}}\Phi_{\mathbf{l},\mathbf{j}} := \left(\delta_{t,h_{l_t}}^{0}\Phi_{\mathbf{l},\mathbf{j}}\right)_{t=1,\dots,d}, \tag{62}$$

$\delta_{t,h_{l_t}}^{-}$, $\delta_{t,h_{l_t}}^{+}$ are left-sided, right-sided differences and $\delta_{t,h_{l_t}}^{0}$ is centered difference defined in equation (39).

(SG4) The electric field is evaluated at particle positions using the combination technique; each partial representation of the field is interpolated using the sparse interpolation functions and combined according to the following formula:

$$\mathbf{E}_n^m(\mathbf{x}_p) := \sum_{\sigma=0}^{d-1}(-1)^\sigma \binom{d-1}{\sigma} \sum_{\mathbf{l}\in\mathcal{L}(n,\sigma)} \underbrace{\sum_{\mathbf{j}\in\mathcal{J}_\mathbf{l}} \alpha_{\mathbf{l},\mathbf{j}}\phi_{\mathbf{l},\mathbf{j}}^m(\mathbf{x}_p)}_{\mathbf{E}_\mathbf{l}^m(\mathbf{x}_p)}, \tag{63}$$

where $\mathbf{E}_\mathbf{l}^m(\mathbf{x}_p)$ is the electric field interpolant on the sub-grid of level $\mathbf{l}$, $\mathcal{L}(n,\sigma)$, $\mathcal{J}_\mathbf{l}$ are defined in equations (22), (17) and the coefficients $\alpha_{\mathbf{l},\mathbf{j}}$ are determined by the interpolation conditions:

$$\forall \mathbf{j}\in\mathcal{J}_\mathbf{l}, \quad \mathbf{E}_\mathbf{l}^m(\mathbf{x}_{\mathbf{l},\mathbf{j}}) = \sum_{\tilde{\mathbf{j}}\in\mathcal{J}_\mathbf{l}} \alpha_{\mathbf{l},\tilde{\mathbf{j}}}\phi_{\mathbf{l},\tilde{\mathbf{j}}}^m(\mathbf{x}_{\mathbf{l},\mathbf{j}}) = \mathbf{E}_{\mathbf{l},\mathbf{j}}. \tag{64}$$

Proposition 3.11. *Assuming enough smoothness on ρ so that $\Phi \in X_{\mathbf{5},0}(\gamma)$, $\rho \in X_\mathbf{5}(\kappa)$, the sparse grid interpolant of the electric field converges to the exact solution in L^p norm, $1 \le p \le \infty$, according to the following estimation:*

$$\|\boldsymbol{E}_n^m - \boldsymbol{E}\|_p = \mathcal{O}\left(\underbrace{h_n^2}_{\mathcal{G}_n^\parallel} + \underbrace{log_2(h_n^{-1})^{d-1}h_n^2}_{\mathcal{G}_n^\times} + \underbrace{log_2(h_n^{-1})^{d-1}(Nh_n)^{-\frac{1}{2}}}_{\mathcal{P}_{n,N}} \right), \tag{65}$$

where $\boldsymbol{E} = -\nabla\Phi$, $\Delta\Phi = -\rho/\varepsilon_0$. In the two dimensional case with B1-splines, we have the following estimation on the sparse grid interpolant of the electric field:

$$\begin{aligned}
\|\boldsymbol{E}_n^m - \boldsymbol{E}\|_p \le & \left(\frac{1}{96}(\|\nabla\partial_x^2\rho\|_\infty + \|\nabla\partial_y^2\rho\|_\infty + \|\nabla\partial_x^4\Phi\|_\infty + \|\nabla\partial_y^4\Phi\|_\infty)\right. \\
& + \frac{1}{3}\begin{pmatrix} \|\partial_x^3\Phi\|_\infty \\ \|\partial_y^3\Phi\|_\infty \end{pmatrix} + \frac{1}{8}\left(\|\nabla\partial_x^2\Phi\|_\infty + \|\nabla\partial_y^2\Phi\|_\infty\right) \\
& + \left(\sum_{\sigma=0}^{1}(-1)^\sigma h_1^{2(1-\sigma)} \sum_{l\in\mathcal{L}(n,\sigma)} \|\boldsymbol{\Delta}_{h_l}^{-1}\|_\infty\right) \\
& \cdot \left(\frac{1}{1152}(2\|\nabla\partial_x^4\partial_y^4\Phi\|_\infty\|\nabla\partial_x^2\partial_y^4\rho\|_\infty + \|\nabla\partial_x^4\partial_y^2\rho\|_\infty)\right. \\
& \left.\left. + \frac{1}{144}(\|\nabla\partial_x^2\partial_y^2\rho\|_\infty) + \frac{1}{64}(\|\nabla\partial_x^2\partial_y^2\Phi\|_\infty)\right)\right) h_n^2 \\
& + \frac{2}{3}\left(\sum_{\sigma=0}^{1}(-1)^\sigma h_1^{-(1-\sigma)/2} \sum_{l\in\mathcal{L}(n,\sigma)} \|\boldsymbol{\Delta}_{h_l}^{-1}\|_\infty\right)\left(\frac{\mathcal{Q}}{Nh_n}\right)^{\frac{1}{2}} \|\nabla\rho\|_\infty^{\frac{1}{2}},
\end{aligned} \tag{66}$$

where $\Delta_{h_l}^{-1}$ is the inverse matrix of the Laplacian problem defined in equation (69).

Remark 3.12. The estimation of the error requires stronger assumptions on the smoothness of the density ($\rho \in X_\mathbf{5}(\kappa)$) than for the HG scheme ($\rho \in X_\mathbf{3}(\kappa)$). The significative differences with the HG scheme are the additional $\mathcal{G}_n^\times$ terms depending on $\|\nabla\partial_x^2\partial_y^4\rho\|_\infty$, $\|\nabla\partial_x^4\partial_y^2\rho\|_\infty$, $\|\nabla\partial_x^4\partial_y^4\Phi\|_\infty$ which are seventh order derviatives of the density and ninth order derivatives of the potential. In comparison, the dominant terms in the HG scheme estimation in equation (47) are third order for the density and fifth order for the potential.

Proposition 3.13. *Assuming Poisson equation is supplemented with periodic boundary conditions and the electric field is interpolated at particle positions using B1-splines, the scheme does preserve the total momentum of the system, i.e*

$$\frac{d\mathcal{P}}{dt} = 0, \tag{67}$$

where $\mathcal{P} = m\mathcal{N}\iint \boldsymbol{v}\tilde{f}_N(\boldsymbol{x},\boldsymbol{v},t)d\boldsymbol{x}d\boldsymbol{v}, \quad \tilde{f}_N(\boldsymbol{x},\boldsymbol{v},t) = \sum_{p=1}^{N}\frac{1}{N}\delta(\boldsymbol{x}-\boldsymbol{x}_p(t))\delta(\boldsymbol{v}-\boldsymbol{v}_p(t)).$

Proof of proposition 3.11. The proof is given with B1-splines. In order to apply the proposition 3.2 and lemma 3.4 that will give us the result, we need to verify the assumptions of equations (26) and (34). Let $\mathbf{l} = (l_1, l_2)$, the partition of unit property of basis functions provides:

$$\mathbf{E}_{\mathbf{l}}^m(\mathbf{x}) - \mathbf{E}(\mathbf{x}) = \sum_{\mathbf{j}\in\mathcal{J}_{\mathbf{l}}}(\mathbf{E}_{\mathbf{l},\mathbf{j}} - \mathbf{E}(\mathbf{x}_{\mathbf{l},\mathbf{j}}) + \mathbf{E}(\mathbf{x}_{\mathbf{l},\mathbf{j}}) - \mathbf{E}(\mathbf{x}))\phi_{\mathbf{l},\mathbf{j}}^m(\mathbf{x}). \tag{68}$$

The first term $\mathbf{E}_{\mathbf{l},\mathbf{j}} - \mathbf{E}(\mathbf{x}_{\mathbf{l},\mathbf{j}})$ is the field solver error resulting from the two discrete finite difference operators $\nabla_{h_{\mathbf{l}}}$ and $\Delta_{h_{\mathbf{l}}}$. Unlike the problem discretized on the Cartesian grid (see proof of proposition 3.10), the resolution of the Poisson equation on the sub-grids requires more work because of the anisotropy of the grids, the matrix of the problem $\boldsymbol{\Delta}_{h_{\mathbf{l}}}$ depending on h_{l_1} and h_{l_2}. Thus, invertibility of the matrix cannot provide directly an error expansion of the form of equations (26),(34). This problem has been thoroughly studied in [25, 21]. We therefore use the framework introduced in [25] for this proof. In the following, we consider a matrix notation introduced in the proof of proposition 3.10 and omit the dependence of the grid discretization in the notations since the functions are implicitly evaluated at the grid nodes. The discrete Poisson problem in matrix notation is:

$$\boldsymbol{\Delta}_{h_{\mathbf{l}}}\boldsymbol{\Phi} = -\boldsymbol{\rho}, \qquad \boldsymbol{\Delta}_{h_{\mathbf{l}}} = \begin{pmatrix} -A_{l_1,l_2} & I_{l_1} & 0 & \cdots & 0 \\ I_{l_1} & -A_{l_1,l_2} & I_{l_1} & & \\ \vdots & \ddots & \ddots & \ddots & \vdots \\ & & I_{l_1} & -A_{l_1,l_2} & I_{l_1} \\ 0 & \cdots & 0 & I_{l_1} & -A_{l_1,l_2} \end{pmatrix}, \tag{69}$$

where A_{l_1,l_2} is a tridiagonal matrix such that $(A_{l_1,l_2})_{i,i} = 2h_{l_1}^{-1} + 2h_{l_2}^{-1}$, $A_{i+1,i} = A_{i,i+1} = -h_{l_2}^{-1}$ and I_{l_1} is the diagonal matrix such that $(I_{l_1})_{i,j} = \delta_{i,j}h_{l_1}^{-1}$. Assuming enough smoothness on the potential $\Phi \in X_{\mathbf{5},0}(\gamma)$, with a Taylor expansion the truncation error of the problem is:

$$\begin{aligned} &\boldsymbol{\Delta}_{h_{\mathbf{l}}}\boldsymbol{\Phi} + \boldsymbol{\rho} = \boldsymbol{\sigma}_1^{(\Delta)}h_{l_1}^2 + \boldsymbol{\sigma}_2^{(\Delta)}h_{l_2}^2 \\ \Leftrightarrow\ &\boldsymbol{\Delta}_{h_{\mathbf{l}}}\boldsymbol{\Phi} + \boldsymbol{\rho}_{\mathbf{l},\mathbf{j},N} = \boldsymbol{\rho}_{\mathbf{l},\mathbf{j},N} - \boldsymbol{\rho} + \boldsymbol{\sigma}_1^{(\Delta)}h_{l_1}^2 + \boldsymbol{\sigma}_2^{(\Delta)}h_{l_2}^2 \\ \Leftrightarrow\ &\boldsymbol{\Delta}_{h_{\mathbf{l}}}\boldsymbol{\Phi} + \boldsymbol{\rho}_{\mathbf{l},\mathbf{j},N} = (\boldsymbol{\tau}_1 + \boldsymbol{\sigma}_1^{(\Delta)})h_{l_1}^2 + (\boldsymbol{\tau}_2 + \boldsymbol{\sigma}_2^{(\Delta)})h_{l_2}^2 + \boldsymbol{\tau}_{1,2}h_{l_1}^2h_{l_2}^2 \\ &\qquad\qquad + \boldsymbol{\zeta}_{1,2}(Nh_{l_1}h_{l_2})^{-\frac{1}{2}}. \end{aligned} \tag{70}$$

where $\sigma_1^{(\Delta)} = \frac{1}{12}\partial_x^4\Phi$, $\sigma_2^{(\Delta)} = \frac{1}{12}\partial_y^4\Phi$, are the truncation expansions in each dimension and τ_1, τ_2, $\tau_{1,2}$, $\zeta_{1,2}$ are the bias and variance coefficients defined in equations (32),(33). Following [25], the auxiliary semi-discrete problems are introduced:

$$\boldsymbol{\Delta}_{h_1}^{(l_1)}\boldsymbol{\omega}_1 = (\boldsymbol{\tau}_1 + \boldsymbol{\sigma}_1^{(\Delta)}), \quad \boldsymbol{\Delta}_{h_1}^{(l_2)}\boldsymbol{\omega}_2 = (\boldsymbol{\tau}_2 + \boldsymbol{\sigma}_2^{(\Delta)}), \tag{71}$$

where $\omega_1(\cdot;h_{l_1})$, $\omega_2(\cdot;h_{l_2})$ are defined on the following hyper-planes:

$$\Omega_{\mathbf{l}}^{(l_1,\dots,l_m)} := \left\{\mathbf{x}\in\Omega \mid x_t \in \{jh_{l_t} \mid 0\le j\le h_{l_t}^{-1}\}, 1\le t\le m\right\}, \tag{72}$$

and $\Delta_{h_{\mathbf{l}}}^{(l_1)}$, $\Delta_{h_{\mathbf{l}}}^{(l_2)}$ are the semi-discrete operators:

$$\Delta_{h_{\mathbf{l}}}^{(l_1)} := \delta_{1,h_{l_1}}^{+}\delta_{1,h_{l_1}}^{-} + \partial_y^2, \quad \Delta_{h_{\mathbf{l}}}^{(l_2)} := \partial_x^2 + \delta_{2,h_{l_2}}^{+}\delta_{2,h_{l_2}}^{-}. \tag{73}$$

From [25, Lemma 3.1, 2.], a semi-discrete maximum principle holds, giving:

$$\left\|\partial_y^4\omega_t(\cdot;h_{l_t})\right\|_\infty \le \frac{1}{8}\left\|\partial_y^4(\tau_t+\sigma_t^{(1)})(\cdot;h_{l_t})\right\|_\infty, \quad t=1,2. \tag{74}$$

The truncation error can be rescast into:

$$\begin{aligned}\boldsymbol{\Delta}_{h_{\mathbf{l}}}(\boldsymbol{\Phi}-\boldsymbol{\omega}_1h_{l_1}^2-\boldsymbol{\omega}_2h_{l_2}^2)+\boldsymbol{\rho}_{\mathbf{l},\mathbf{j},N} &= (\boldsymbol{\Delta}_{h_{\mathbf{l}}}^{(l_1)}-\boldsymbol{\Delta}_{h_{\mathbf{l}}})\boldsymbol{\omega}_1h_{l_1}^2+(\boldsymbol{\Delta}_{h_{\mathbf{l}}}^{(l_2)}-\boldsymbol{\Delta}_{h_{\mathbf{l}}})\boldsymbol{\omega}_2h_{l_2}^2\\ &\quad+\boldsymbol{\tau}_{1,2}h_{l_1}^2h_{l_2}^2+\boldsymbol{\zeta}_{1,2}(Nh_{l_1}h_{l_2})^{-\frac{1}{2}}.\end{aligned}$$

From [25, Lemma 3.2, 2.], we have the result:

$$(\boldsymbol{\Delta}_{h_{\mathbf{l}}}^{(l_1)}-\boldsymbol{\Delta}_{h_{\mathbf{l}}})\boldsymbol{\omega}_{l_1} = \boldsymbol{\omega}_{1,2}^{\star}h_{l_2}^2, \quad (\boldsymbol{\Delta}_{h_{\mathbf{l}}}^{(l_2)}-\boldsymbol{\Delta}_{h_{\mathbf{l}}})\boldsymbol{\omega}_2 = \boldsymbol{\omega}_{2,1}^{\star}h_{l_1}^2, \tag{75}$$

with bounded $\|\omega_{1,2}^{\star}(\cdot;h_{l_1},h_{l_2})\|_\infty \le \frac{1}{12}\left\|\partial_y^4\omega_1(\cdot;h_{l_1})\right\|_\infty$,
$\|\omega_{2,1}^{\star}(\cdot;h_{l_2},h_{l_1})\|_\infty \le \frac{1}{12}\left\|\partial_x^4\omega_2(\cdot;h_{l_2})\right\|_\infty$. Owing to invertibility of $\boldsymbol{\Delta}_{h_{\mathbf{l}}}$, we get:

$$\begin{aligned}\boldsymbol{\Phi}-\underbrace{(-\boldsymbol{\Delta}_{h_{\mathbf{l}}}^{-1}\boldsymbol{\rho}_{\mathbf{l},\mathbf{j},N})}_{\boldsymbol{\Phi}_{\mathbf{l},\mathbf{j}}} &= \boldsymbol{\omega}_1h_{l_1}^2+\boldsymbol{\omega}_2h_{l_2}^2+\boldsymbol{\Delta}_{h_{\mathbf{l}}}^{-1}\Big((\boldsymbol{\omega}_{1,2}^{\star}+\boldsymbol{\omega}_{2,1}^{\star}+\boldsymbol{\tau}_{1,2})h_{l_1}^2h_{l_2}^2\\ &\quad+\boldsymbol{\zeta}_{1,2}(Nh_{l_1}h_{l_2})^{-\frac{1}{2}}\Big).\end{aligned} \tag{76}$$

Using Taylor expansions and substracting them, the error of the discrete gradient operator is:

$$\nabla\boldsymbol{\Phi}-\nabla_{h_{\mathbf{l}}}\boldsymbol{\Phi} = \begin{pmatrix}\boldsymbol{\sigma}_1^{(\nabla)}h_{l_1}^2\\ \boldsymbol{\sigma}_2^{(\nabla)}h_{l_2}^2\end{pmatrix}+\mathcal{O}(h_{l_1}^4,h_{l_2}^4). \tag{77}$$

where $\sigma_1^{(\nabla)} = \frac{1}{3}\partial_x^3\Phi$, $\sigma_2^{(\nabla)} = \frac{1}{3}\partial_y^3\Phi$. Since $\Phi\in X_{\mathbf{5},0}(\gamma)$, $\rho\in X_{\mathbf{5}}(\kappa)$, we have $\omega_1,\omega_2,\omega_{1,2}^{\star},\omega_{2,1}^{\star},\tau_{1,2},\zeta_{1,2}\in X_{\mathbf{1}}$. A Taylor expansion at grid nodes provides:

$$\nabla_{h_{\mathbf{l}}}\boldsymbol{\omega} = \nabla\boldsymbol{\omega}+\mathcal{O}(h_{l_1}^2,h_{l_2}^2), \tag{78}$$

where ω denotes any of the functions $\omega_1,\omega_2,\omega_{1,2}^{\star},\omega_{2,1}^{\star},\tau_{1,2},\zeta_{1,2}$. Owing to the commutativity of $\boldsymbol{\Delta}_{h_{\mathbf{l}}}^{-1}$ and $\boldsymbol{\nabla}_{h_{\mathbf{l}}}$, applying $-\nabla_{h_{\mathbf{l}}}$ to equation (76) and summing to equation (77):

$$\mathbf{E}_{\mathbf{l},\mathbf{j}}-\mathbf{E} = \begin{pmatrix}(\nabla\boldsymbol{\omega}_1+\boldsymbol{\sigma}_1^{(\nabla)})h_{l_1}^2+\nabla\boldsymbol{\omega}_2h_{l_2}^2+\Theta_{h_{l_1},h_{l_2}}\\ \nabla\boldsymbol{\omega}_1h_{l_1}^2+(\nabla\boldsymbol{\omega}_2+\boldsymbol{\sigma}_2^{(\nabla)})h_{l_2}^2+\Theta_{h_{l_1},h_{l_2}}\end{pmatrix}, \tag{79}$$

where $\Theta_{h_{l_1},h_{l_2}} = \boldsymbol{\Delta}_{h_{\mathbf{l}}}^{-1}\left((\nabla\boldsymbol{\omega}_{1,2}^{\star}+\nabla\boldsymbol{\omega}_{2,1}^{\star}+\nabla\boldsymbol{\tau}_{1,2})h_{l_1}^2h_{l_2}^2+\nabla\boldsymbol{\zeta}_{1,2}(Nh_{l_1}h_{l_2})^{-\frac{1}{2}}\right)$. Then, using the notation introduced in equation (55) for each function $\nabla\omega_1$, $\nabla\omega_2$, $\sigma_1^{(\nabla)}$, $\sigma_2^{(\nabla)}$, $\nabla\omega_{1,2}^{\star}$, $\nabla\omega_{2,1}^{\star}$, $\nabla\tau_{1,2}$, $\nabla\zeta_{1,2}$, the sum over the two first terms in equation (68)

verifies the assumptions of equations (26),(34). Taylor expanding the field $\mathbf{E}$ similarly to equation (49):

$$\sum_{\mathbf{j}\in\mathcal{J}_\mathbf{l}}(\mathbf{E}(\mathbf{x}_{\mathbf{l},\mathbf{j}})-\mathbf{E}(\mathbf{x}))\phi^m_{\mathbf{l},\mathbf{j}}(\mathbf{x}) = \xi_1(\mathbf{x};h_{l_1})h_{l_1}^2+\xi_2(\mathbf{x};h_{l_2})h_{l_2}^2+\xi_{1,2}(\mathbf{x};h_{l_1},h_{l_2})h_{l_1}^2h_{l_2}^2 + \mathcal{O}(h_{l_1}^4,h_{l_2}^4),$$

where $\xi_1,\xi_2,\xi_{1,2}$ are the interpolation error functions, verifying $\|\xi_1(\cdot;h_{l_1})\|_\infty \leq \kappa/8$, $\|\xi_2(\cdot;h_{l_2})\|_\infty \leq \kappa/8$, $\|\xi_{1,2}(\cdot;h_{l_1},h_{l_2})\|_\infty \leq \kappa/64$ and notations introduced in equations (51), (52):

$$\begin{aligned} &h_{l_1}^2\xi_1(\mathbf{x};h_{l_1}) = \frac{1}{2}\delta_1^\star(h_{l_1}-\delta_1^\star)\partial_x^2\mathbf{E}(\mathbf{x}), \quad h_{l_2}^2\xi_2(\mathbf{x};h_{l_2}) = \frac{1}{2}\delta_2^\star(h_{l_2}-\delta_2^\star)\partial_y^2\mathbf{E}(\mathbf{x}),\\ &h_{l_1}^2h_{l_2}^2\xi_{1,2}(\mathbf{x};h_{l_1},h_{l_2}) = \frac{1}{4}\delta_1^\star\delta_2^\star(h_{l_1}-\delta_1^\star)(h_{l_2}-\delta_2^\star)\partial_x^2\partial_y^2\mathbf{E}(\mathbf{x}).\end{aligned} \tag{80}$$

We conclude using proposition 3.2, lemma 3.4 and, thanks to the boundedness of matrix $\mathbf{\Delta}_{h_\mathbf{l}}^{-1}$, as well as functions $\nabla\tilde{\omega}_1,\nabla\tilde{\omega}_2,\tilde{\sigma}_1^{(\nabla)},\tilde{\sigma}_2^{(\nabla)},\nabla\tilde{\omega}^\star_{1,2},\nabla\tilde{\omega}^\star_{2,1}$, $\nabla\tilde{\tau}_{1,2},\nabla\tilde{\zeta}_{1,2},\xi_1,\xi_2,\xi_{1,2}$:

$$\begin{aligned}\|\mathbf{E}_n^m-\mathbf{E}\|_p \leq &\left(\frac{\kappa+29\gamma}{48}+\left(\sum_{\sigma=0}^1(-1)^\sigma h_1^{2(1-\sigma)}\Gamma_n\right)\left(\frac{5\kappa+10\gamma}{576}\right)\right)h_n^2\\ &+\left(\sum_{\sigma=0}^1(-1)^\sigma h_1^{-(1-\sigma)/2}\Gamma_n\right)\frac{2\mathcal{Q}}{3}(Nh_n)^{-\frac{1}{2}},\end{aligned} \tag{81}$$

where $\Gamma_n := \sum_{\mathbf{l}\in\mathcal{L}(n,\sigma)}\|\mathbf{\Delta}_{h_\mathbf{l}}^{-1}\|_\infty = \mathcal{O}(n)$.

Proof of proposition 3.13. The total momentum of the system is defined as

$$\mathcal{P} = m\iint\mathbf{v}\sum_{p=1}^N\frac{\mathcal{N}}{N}\delta(\mathbf{x}-\mathbf{x}_p(t))\delta(\mathbf{v}-\mathbf{v}_p(t))d\mathbf{x}d\mathbf{v} = \sum_{p=1}^N m\frac{\mathcal{N}}{N}\mathbf{v}_p(t), \tag{82}$$

so

$$\frac{d\mathcal{P}}{dt} = \sum_{p=1}^N m\frac{\mathcal{N}}{N}\frac{d\mathbf{v}_p(t)}{dt} = \sum_{p=1}^N q\frac{\mathcal{N}}{N}\mathbf{E}_n(\mathbf{x}_p(t)), \tag{83}$$

where $\mathbf{E}_n$ is the electric field interpolated at particle positions, given by:

$$\mathbf{E}_n(\mathbf{x}_p(t)) = \sum_{\sigma=0}^1(-1)^\sigma\sum_{\mathbf{l}\in\mathcal{L}(n,\sigma)}\sum_{\mathbf{j}\in\mathcal{J}_\mathbf{l}}\mathbf{E}_{\mathbf{l},\mathbf{j}}\underbrace{\mathcal{S}_{2,\mathbf{l}}(\mathbf{x}_p(t)-\mathbf{x}_{\mathbf{l},\mathbf{j}})h_{l_1}h_{l_2}}_{=\phi^1_{\mathbf{l},\mathbf{j}}(\mathbf{x}_p(t))}, \tag{84}$$

Exchanging the sums, we get:

$$\frac{d\mathcal{P}}{dt} = \sum_{\sigma=0}^1(-1)^\sigma\sum_{\mathbf{l}\in\mathcal{L}(n,\sigma)}h_{l_1}h_{l_2}\sum_{\mathbf{j}\in\mathcal{J}_\mathbf{l}}\mathbf{E}_{\mathbf{l},\mathbf{j}}\underbrace{\frac{\mathcal{Q}}{N}\sum_{p=1}^N\mathcal{S}_{2,\mathbf{l}}(\mathbf{x}_p(t)-\mathbf{x}_{\mathbf{l},\mathbf{j}})}_{=\rho_{\mathbf{l},\mathbf{j},N}}, \tag{85}$$

Let us consider a sub-grid of level $\mathbf{l}$ and the notations $\Phi^\mathbf{j}=\Phi_{\mathbf{l},\mathbf{j}}$, $\mathbf{E}^\mathbf{j}=\mathbf{E}_{\mathbf{l},\mathbf{j}}$, $\rho^\mathbf{j}=\rho_{\mathbf{l},\mathbf{j},N}$ where $\mathbf{j}=(j_1,j_1)\in\mathcal{J}_\mathbf{l}$. Owing to periodic conditions on the field and the

density:

$$\sum_{\mathbf{j}\in\mathcal{J}_\mathbf{l}} \mathbf{E}^\mathbf{j}\rho^\mathbf{j} = \sum_{\mathbf{j}\in\mathcal{J}_\mathbf{l}} \nabla_{h_\mathbf{l}}\Phi^\mathbf{j}\Delta_{h_\mathbf{l}}\Phi^\mathbf{j}$$
$$= \sum_{j_1=0}^{2^{l_1}}\sum_{j_2=0}^{2^{l_2}} \left(\frac{2\Phi^{j_1,j_2}\Phi^{j_1+1,j_2} - (\Phi^{j_1+1,j_2})^2 + (\Phi^{j_1-1,j_2})^2 - 2\Phi^{j_1,j_2}\Phi^{j_1-1,j_2}}{2h_{l_1}^3} \right)$$
$$+ \left(\frac{2\Phi^{j_1,j_2}\Phi^{j_1,j_2+1} - (\Phi^{j_1,j_2+1})^2 + (\Phi^{j_1,j_2-1})^2 - 2\Phi^{j_1,j_2}\Phi^{j_1,j_2-1}}{2h_{l_2}^3} \right).$$

A change of index together with the periodicity of the problem yields:

$$\sum_{j_1=0}^{2^{l_1}} 2\Phi^{j_1,j_2}\Phi^{j_1+1,j_2} = \sum_{j_1=0}^{2^{l_1}} 2\Phi^{j_1,j_2}\Phi^{j_1-1,j_2}, \qquad \sum_{j_1=0}^{2^{l_1}} (\Phi^{j_1-1,j_2})^2 = \sum_{j_1=0}^{2^{l_1}} (\Phi^{j_1+1,j_2})^2$$

Thus, owing to equivalent relations in j_2,

$$\frac{d\mathcal{P}}{dt} = 0. \ \square$$

Remark 3.14. The proof on the conservation of the total momentum is not applicable to the HG scheme. Indeed, the source term of the Poisson equation does not appear in the field expression in equation (85).

3.3. **Offset combination technique.** From the analysis conducted in the precedent sections, the following conclusions may be stated. Sparse grid reconstructions define a different trade off between the three components of the errors (grid-based and particle sampling errors) as compared to standard PIC approximations. The particle sampling error is significantly mitigated thanks to sparse grid approximations. This is an important feature since this component of the error is generally the most detrimental for the computations and ultimately limits the precision of the approximation. Contrariwise, the grid-based error is less favorable for the sparse grid approximations: the component $\mathcal{G}_n^\times$ is increased and dominates the grid based error (see tables 1a, 1b for a comparison of the methods). In this section, a general

Table 1. Grid-based error: dependances of the error components $\mathcal{G}_n^\parallel$ and $\mathcal{G}_n^\times$ with respect to the grid size (h_n) and the solution regularity (derivatives, $t = 1, ..., d$).

(a) Density grid based error ($\|\rho_{n,N}^m - \rho\|_p$).

Scheme	$\mathcal{G}_n^\parallel$ (grid)	$\mathcal{G}_n^\parallel$ (solution)	$\mathcal{G}_n^\times$ (grid)	$\mathcal{G}_n^\times$ (solution)
STD	$\mathcal{O}(h_n^2)$	$\|\nabla\partial_t^2\rho\|_\infty$	$\mathcal{O}(h_n^4)$	$\|\nabla\partial_1^2...\partial_d^2\rho\|_\infty$
HG/SG	$\mathcal{O}(h_n^2)$	$\|\nabla\partial_t^2\rho\|_\infty$	$\mathcal{O}(\log_2(h_n^{-1})^{d-1}h_n^2)$	$\|\nabla\partial_1^2...\partial_d^2\rho\|_\infty$

(b) Electric field grid based error ($\|\mathbf{E}_n^m - \mathbf{E}\|_p$).

Scheme	$\mathcal{G}_n^\parallel$ (grid)	$\mathcal{G}_n^\parallel$ (solution)	$\mathcal{G}_n^\times$ (grid)	$\mathcal{G}_n^\times$ (solution)
STD	$\mathcal{O}(h_n^2)$	$\|\nabla\partial_t^4\Phi\|_\infty$, $\|\nabla\partial_t^2\rho\|_\infty$	$\mathcal{O}(h_n^4)$	$\|\nabla\partial_1^4...\partial_d^4\Phi\|_\infty$, $\|\nabla\partial_1^2...\partial_d^2\rho\|_\infty$
HG	$\mathcal{O}(h_n^2)$	$\|\nabla\partial_t^4\Phi\|_\infty$, $\|\nabla\partial_t^2\rho\|_\infty$	$\mathcal{O}(\log_2(h_n^{-1})^{d-1}h_n^2)$	$\|\nabla\partial_1^2...\partial_d^2\rho\|_\infty$
SG	$\mathcal{O}(h_n^2)$	$\|\nabla\partial_t^4\Phi\|_\infty$, $\|\nabla\partial_t^2\rho\|_\infty$	$\mathcal{O}(\log_2(h_n^{-1})^{d-1}h_n^2)$	$\|\nabla\partial_1^4...\partial_d^4\Phi\|_\infty$, $\|\nabla\partial_1^2\partial_2^4...\partial_d^4\rho\|_\infty$, ..., $\|\nabla\partial_1^4\partial_2^4...\partial_d^2\rho\|_\infty$

framework, that we shall referred to as offset combination technique, is introduced

in order to reduce the grid based error of sparse grid reconstructions. The offset combination technique is motivated by the property of the error $\mathcal{G}_n^\times$ to be an increasing function of the number of sub-grids involved in the combination ($\mathcal{O}(n^{d-1})$) as well as the combined sum of the errors of the partial estimators. The offset combination consists therefore in both reducing the number of sub-grids considered within the combination and using sub-grids with increased minimum levels. In this respect, the offset combination borrows some ideas to the so-called truncated combination [28, 2]. However, a more subtle strategy is implemented within the offset combination in order to select efficiently the subset of sub-grids.

The main drawback of the truncated method is the additional statistical error introduced in the simulation, because of the smaller cells of the grids considered in the combination, the mean number of particles per cell is reduced. The offset combination is aimed at mitigating the increase of the statistical noise as well as the dominant component of the grid based error $\mathcal{G}_n^\times$ in return of a deterioration of the component $\mathcal{G}_n^\parallel$. The method is presented in this section for an equidistant grid Ω_n, but can be extended to any non-equidistant grid $\Omega_{\mathbf{n}}$, $\mathbf{n} = (n_1, ..., n_d)$. The tuning of the balance between the different components of the error is implemented thanks to the two parameters $l^0, l^1 \in \mathbb{N}$. The index l^0 is used to parametrized the minimum discretization level for the sub-grids, with the aim to discard the most anisotropic sub-grids from the combination. The parameter l^1 sets the loss of discretization in the directions aligned with the axis (contributing to the $\mathcal{G}_n^\parallel$ grid-based error). Let $l^1 = 0$ the offset method boils down to the truncated combination technique introduced in [2, 28]. Let us introduce notations for the method: the discretization in the directions aligned with the axis is denoted $n_\parallel$, the discretization in the cross directions is denoted $n_\times$ and n_{sg} refers to the number of sub-grids in the combination[1]

$$n_\parallel := n - l^1, \qquad n_\times := n + (d-1)l^0 - l^1, \qquad n_{sg} := n - l^0 - l^1. \tag{87}$$

The sub-grids of the offset combination are defined by the subset of indices[2], denoted $\mathcal{L}(n, l^0, l^1, \sigma)$ and defined as:

$$\mathbf{l} = (l_1, ..., l_d) \in \mathcal{L}(n, l^0, l^1, \sigma) := \left\{ \mathbf{l} \in \mathbb{N}^d \mid \mathbf{l} > \mathbf{l}^0, \; |\mathbf{l}|_1 = n_\times + d - 1 - \sigma \right\}, \tag{88}$$

where $\sigma \in \{0, ..., d-1\}$.

[1] The number of sub-grids considered in the offset combination technique, denoted $\mathcal{N}_{sg}$, is:

$$\mathcal{N}_{sg} = \begin{cases} 2n_{sg} - 1 & \text{if } d = 2, \\ 2n_{sg}^2 - 2n_{sg} + 1 & \text{if } d = 3. \end{cases} \tag{86}$$

[2] As an example, for

$$\begin{cases} n = 7, & l^0 = 2, & l^1 = 1 & \text{(offset)}, \\ n = 7, & l^0 = 2, & l^1 = 0 & \text{(truncated)}; \end{cases}$$

the combination consists of the sub-grids with the following level set:

$$\begin{cases} \bigcup\limits_{0 \le \sigma \le d-1} \mathcal{L}(n, l^0, l^1, \sigma) & = \{(6,3), (5,4), (4,5), (3,6), (5,3), (4,4), (3,5)\}, \\ \bigcup\limits_{0 \le \sigma \le d-1} \mathcal{L}(n, l^0, l^1, \sigma) & = \{(7,3), (6,4), (5,5), (4,6), (3,7), (6,3), (5,4), \\ & \qquad (4,5), (3,6)\}. \end{cases}$$

Proposition 3.15. *The density interpolant issued from the offset combination applied to the HG-scheme converges in L^p-norms, $1 \leq p \leq \infty$ with*

$$\|\rho^m_{n,N} - \rho\|_p = \mathcal{O}\left(\underbrace{h^2_{n_\parallel}}_{\mathcal{G}^\parallel_n} + \underbrace{log_2(h^{-1}_{n_{sg}})^{d-1} h^2_{n_\times}}_{\mathcal{G}^\times_n} + \underbrace{log_2(h^{-1}_{n_{sg}})^{d-1} N h^{-\frac{1}{2}}_{n_\times}}_{\mathcal{P}_{n,N}} \right). \tag{89}$$

where $n_\parallel, n_\times$ and n_{sg} are defined in equations (87).

Compared to the estimation of the HG scheme (equation (44)) both the grid-based component $\mathcal{G}^\times_n$ and the particle sampling component $\mathcal{P}_{n,N}$ of the error are mitigated in the offset method. This is obtained thanks to the reduced number of sub-grids in the combination which scales with $\mathcal{O}(n^{d-1}_{sg})$ instead of $\mathcal{O}(n^{d-1})$, $n_{sg} \leq n$. Besides, the use of sub-grids with higher levels, *i.e.* parametrized by indices $\mathbf{l}$ with larger $|\mathbf{l}|_1$, entails an offset for both $\mathcal{P}_{n,N}$ and $\mathcal{G}^\times_n$, if $n_\times > n$. Conversely, the component $\mathcal{G}^\parallel_n$ is increased by the elimination of the more anisotropic grids because $n_\parallel < n$ if $l^1 > 0$, however this is of no consequence on the accuracy of the numerical method since the grid based error is dominated by the component $\mathcal{G}^\times_n$.

Remark 3.16. The offset combination technique can be applied to either the HG scheme or the SG scheme without the loss of their conservativity properties (total charge, total momentum, etc.) but with the same improvements with respect to the precision.

3.4. **Enhancements of the hybrid grid and sub-grid schemes.**

3.4.1. *Objectives.* The analyses conducted within section 3.2 highlight a deterioration of the electric field approximations carried out by sparse grid PIC methods (see table 1b) compared to standard PIC methods. Similarly to the density interpolant, this altered precision, more important for the SG-Scheme, is due to an increase of the grid based error component $\mathcal{G}^\times_n$ depending on high order cross derivatives of the solution. The corrections proposed herein address this specific issue.

3.4.2. *Oversampled hybrid grid (OHG scheme).* The HG scheme does not take advantage of sparse-grid techniques for the resolution of the electric field, the potential being carrying out on a Cartesian mesh, unlike the SG scheme. This computation may be expansive for refined discretizations and particularly for three dimensional problems. The benefit of this approach is a reduced dependency of the electric field approximation to the solution cross derivatives (compared to the SG-Scheme, see table 1b). The strategy introduced to alleviate the numerical cost of the electric field computation, consists in using grids with different resolutions for the density the density deposition and the electric field computation. Precisely, the electric field is carried out on a Cartesian mesh Ω_n while the density is projected onto a sequence of sub-grids associated to a more refined (oversampled) Cartesian mesh $\Omega_{\tilde{n}}$, where $\tilde{n} = n + \delta_n$, $\delta_n \in \mathbb{N}$. Let us outline the corrected scheme, that we shall name the Oversampled Hybrid grid Particle-In-Cell (OHG) scheme. The steps (OHG1),(OHG2),(OHG4),(OHG5) are similar to respectively the steps (STD1),(HG2),(HG3),(HG4), but the refined Cartesian grid $\Omega_{\tilde{n}}$ is considered at step (OHG2).

(OHG3) The density is deposited onto Ω_n from the values of the sparse grid interpolant on $\Omega_{\tilde{n}}$:

$$\forall \mathbf{j} \in \mathcal{J}_n, \quad \rho^m_{n,N}(\mathbf{x}_{n,\mathbf{j}}) := \frac{\omega_{\tilde{n}}}{\omega_n} \sum_{\tilde{\mathbf{j}} \in \mathcal{J}_{\tilde{n}}} \rho^m_{\tilde{n},N}(\mathbf{x}_{\tilde{n},\tilde{\mathbf{j}}}) \phi_{n,\mathbf{j}}(\mathbf{x}_{\tilde{n},\tilde{\mathbf{j}}}), \tag{90}$$

where $\omega_n, \omega_{\tilde{n}}$ correspond to the volume of a cell of the grids Ω_n and $\Omega_{\tilde{n}}$[3]:

$$\omega_n = \left(\sum_{\mathbf{j} \in \mathcal{J}_n} 1 \right)^{-1}, \quad \omega_{\tilde{n}} = \left(\sum_{\tilde{\mathbf{j}} \in \mathcal{J}_{\tilde{n}}} 1 \right)^{-1}. \tag{91}$$

Proposition 3.17. *The total charge of the density is conserved by the projection onto $\Omega_{\tilde{n}}$ and by reconstruction on Ω_n, i.e*

$$\sum_{\tilde{\boldsymbol{j}} \in \mathcal{J}_{\tilde{n}}} \rho^m_{\tilde{n},N}(\boldsymbol{x}_{\tilde{n},\tilde{\boldsymbol{j}}}) \omega_{\tilde{n}} = \mathcal{Q}. \tag{92}$$

Proof of proposition 3.17. The proposition follows from the definitions of the constants $\omega_n, \omega_{\tilde{n}}$ following the proof of proposition 3.6. □

3.4.3. *Enhanced sub-grids (ESG scheme).* This correction consists in enhancing the sub-grids for the resolution of the electric field by introducing sub-grids more refined than those used for the projection of the density. The sub-grids carrying the electric field are related to the levels $\tilde{l}_t = l_t + \delta_n$, (for $t = 1, ..., d$), $\delta_n \in \mathbb{N}$ being a parameter denoting the additional depth of these enhanced sub-grids. Let us outline the corrected scheme, that we shall name Enhanced Sub-Grid Particle-In-Cell (ESG) scheme. The steps (ESG1),(ESG2),(ESG4), (ESG6) are similar to respectively the steps (STD1),(SG2), (SG3) where the enhanced sub-grids are considered, (SG4) .

(ESG3) On each sub-grid, the partial representation of the density is interpolated to the enhanced sub-grid $\Omega_{\tilde{\mathbf{l}}}$ with standard interpolation:

$$\forall \tilde{\mathbf{j}} \in \mathcal{J}_{\tilde{\mathbf{l}}}, \quad \rho_{\tilde{\mathbf{l}},\tilde{\mathbf{j}},N} := \sum_{\mathbf{j} \in \mathcal{J}_{\mathbf{l}}} \alpha_{\mathbf{l},\mathbf{j}} \phi^m_{\mathbf{l},\mathbf{j}}(\mathbf{x}_{\tilde{\mathbf{l}},\tilde{\mathbf{j}}}), \tag{93}$$

where the coefficients $\alpha_{\mathbf{l},\mathbf{j}}$ are determined by interpolation conditions.

(ESG5) The electric field is reconstructed on the non-enhanced sub-grids in a way similar to equation (90).

4. Numerical simulations

4.1. **General settings.** In the following, we consider the electrons immersed in a uniform, immobile, background of ions: $\rho_i(\mathbf{x}) = \mathcal{Q}_e / \int d\mathbf{x}$. The domain is a square $\Omega := [0, L]^d$, whose dimensions depend on the Debye length $L \propto \lambda_D$, $\lambda_D = \sqrt{\varepsilon_0 T_e / q_e n_0}$, with the following charge, mass and temperature for the electrons $q_e = 1.602 \times 10^{-19}$ C, $m_e = 9.109 \times 10^{-31}$ kg, $T_e = 1$ eV. Periodic boundary conditions are considered for the particles, the electric potential and the electric field. The time discretization depends on the plasma frequency: $t, \Delta t \propto \omega_p^{-1}$, $\omega_p = \sqrt{q_e \rho_e / m_e \varepsilon_0}$. The particles are pushed with a leap-frog temporal scheme following the equations of motion.

[3]The ration $\frac{\omega_{\tilde{n}}}{\omega_n}$ can also be defined as follows $\frac{\omega_{\tilde{n}}}{\omega_n} = \left(\sum_{\tilde{\mathbf{j}} \in \mathcal{J}_{\tilde{n}}} \phi_{n,\mathbf{j}}(\mathbf{x}_{\tilde{n},\tilde{\mathbf{j}}}) \right)^{-1}$.

A series of numerical tests is carried out in two dimensional geometries: a Landau damping in both the linear and the non-linear regimes as well as a diocotron instability. These tests are performed with the standard Particle-In-Cell scheme (STD), the sub-grid Particle-In-cell scheme (SG), the hybrid grid Particle-In-cell scheme (HG), the enhanced sub-grid Particle-In-Cell (ESG) scheme and the oversampled hybrid grid Particle-In-Cell scheme (OHG), respectively presented in section 2.2, 3.2.1, 3.2.2, 3.4.3, 3.4.2. The schemes are implemented either with the classical of the offset combination technique. Throughout this section we will refer to the mean number of particle per cell, denoted P_c, relating the amount of statistical noise in the simulation. This quantity depends on the underlying Cartesian grid or the sub-grids used in the combination.

$$P_c = \frac{N}{h_n^{-2}L^2} = N2^{-2n}, \quad P_c = \frac{N}{nh_{n+1}^{-1}L + (n-1)h_n^{-1}L} = \frac{N2^{-n}}{3n-1}, \tag{94}$$

$$P_c = \frac{N}{n_{sg}h_{n_\times+1}^{-1}L + (n_{sg}-1)h_{n_\times}^{-1}L} = \frac{N2^{-n_\times}}{3n_{sg}-1}, \tag{95}$$

where the grid discretization now depends on the domain size ($h_n = 2^{-n}L$) and $n_\times, n_{sg}$ are defined in equations (87). The mean number of particles per cell is therefore provided by equations (94)-(95) for the STD scheme, the SG, HG, ESG, OHG schemes with the classical combination technique and the offset combination technique.

In any of the following test cases, the total charge of the density is exactly conserved (to machine precision $\approx 10^{-16}$) for the STD, HG scheme and OHG schemes with any combination technique which confirms the propositions 3.6, 3.17. Recalling that within the SG or the ESG scheme, because the density is never fully projected onto a grid since we only proceed a partial projection onto each sub-grid and combine the resulting partial electric fields, the conservation of density is therefore not assessed numerically for these schemes.

4.2. **Landau damping.** As a first test case, we consider the evolution in time of a perturbation known as the Landau damping, in the linear and non-linear regimes. When a plasma is slightly perturbed from an equilibrum state, it returns to its equilibrium with an exponential damping. A perturbation in the electron distribution of an equilibrium state is considered:

$$\tilde{f}_e(\mathbf{x},\mathbf{v}) = \frac{1}{2\pi}\left(1+\alpha_1\cos\left(\frac{\beta_1 2\pi x}{L}\right)\right)\left(1+\alpha_2\cos\left(\frac{\beta_2 2\pi y}{L}\right)\right)e^{\frac{-\|\mathbf{v}\|_2^2}{2}}, \tag{96}$$

where $\|\mathbf{v}\|_2 = (v_x^2+v_y^2)^{1/2}$, $\alpha_{1,2}$ is the magnitude and $\beta_{1,2}$ is the period of the perturbation in each dimension.

4.2.1. *Linear regime.* The perturbation considered in the distribution of electrons has to be small enough so that a linear approximation is valid. Under this assumption, the electric field decreases exponentially fast in time according to a damping rate [29]. The motivation here is to recover this damping rate with the different schemes. Let us parametrize the perturbation with $\alpha_1 = \alpha_2 = 0.05$, $\beta_1 = \beta_2 = 1$ in equation (96), $L = 22\lambda_D$, $\Delta t = \frac{1}{20}\omega_p^{-1}$ and the final time $T = 25\omega_p^{-1}$. The grid discretization is chosen so that $h_n \simeq 0.34\lambda_D$, the configuration of the grid and particles is indicated in table 2. Interpolations in the combination technique are

done with B1-splines for all the methods. The numerical results are represented in figure 2 (a). Both the HG, SG, STD schemes agrees well with the damping rate. Besides, there are four times less total particles in the simulation for the sparse grid schemes.

Table 2. Linear Landau damping: Configuration of the methods.

Scheme	Grid size h_n	P_c	N	N_{Std}/N
STD	2^{-6} (64^2 cells)	500	2.048×10^6	1
SG, HG (classical)	2^{-6} (64^2 cells)	500	5.440×10^5	4

4.2.2. *Non-linear regime.* When the perturbation of the equilibrium state is considered large enough to invalidate the linear approximation, the precedent analytic damping rate is not available anymore. In order to assess the efficiency of the methods, the results will be compared to the STD scheme in the same configuration of grid discretization. A larger perturbation than for the linear case is considered with $\alpha_1 = 0.2$, $\alpha_2 = 0.15$, $\beta_1 = 4$, $\beta_2 = 3$ in equation (96) and let $L = 60\lambda_D$, $\Delta t = \frac{1}{20}\omega_p^{-1}$. The grid discretization is chosen so that $h_n \simeq 0.47\lambda_D$, the configuration of the grid, particles and schemes is indicated in table 3. Interpolations in the combination technique are done with B1-splines functions for each of the methods.

Table 3. Non-linear Landau damping: Configuration of the methods.

Scheme	Parameters	Grid size h_n	P_c	N	N_{Ref}/N
Ref (STD)		2^{-7} (128^2 cells)	4000	6.553×10^7	1
STD		2^{-7} (128^2 cells)	1000	1.638×10^7	4
SG, HG (classical)		2^{-7} (128^2 cells)	1000	2.560×10^6	25.6
ESG, OHG (offset)	$(l^0, l^1, \delta_n) = (2, 1, 1)$	2^{-7} (128^2 cells)	1000	2.816×10^6	23.2

A first series of simulations is performed with different grid resolutions (8, 16, 32, 64, 128 cells in each dimension) and numbers of particles per cell ($P_c = 500, 1000$) in order to get a comparison of the projection error between the methods at initial time. It is therefore possible to assess precisely the precision of the density projected onto the grid for the different methods by comparison with the analytic expression of the initial electron density (ρ_{ex}). The error of the density in L^p norm is defined as:

$$\epsilon_p(\rho) := \frac{\|\rho - \rho_{ex}\|_p}{\|\rho_{ex}\|_p}, \quad 1 \leq p \leq \infty \tag{97}$$

where ρ_{ex} is the analytic density at initial time. The integrals in the L^p norm expressions are approximated with a Riemann sum on the Cartesian grid. The numerical results of the error in L^2 norm (ϵ_2) are represented in figure 3 as functions of the number of cells in the Cartesian grid. The results for the SG scheme are not represented because at initial time the scheme is equivalent to the HG scheme. For any of the methods, the precision is limited by the particle sampling error for quite coarse grid resolutions, as soon as the number of cells is larger than 32×32. Though the total number of particles is increased with the mesh refinement, the mean number of particles per cell remains unchanged, which explains the non decreasing error observed on the plots of figure 3. This highlights that, though the number of particles per cell is consequent (1000), it should be increased further to obtain an

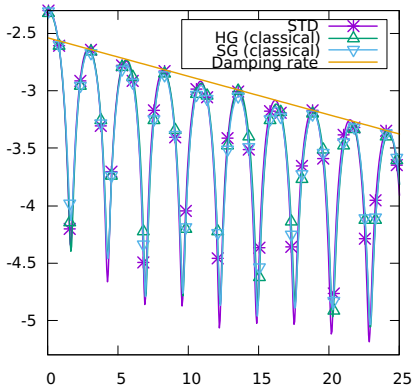

Figure 2. Linear Landau damping: Evolution of the electric field $\|\log(\mathbf{E}_n)\|_{L^2}$ untill $T = 25\omega_p^{-1}$.

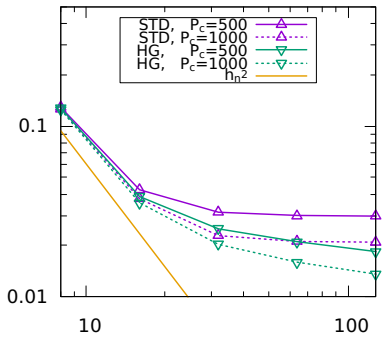

Figure 3. Non-linear Landau damping: $\epsilon_2(\rho_e)$ as a function of the nb. of cells (in each dimension).

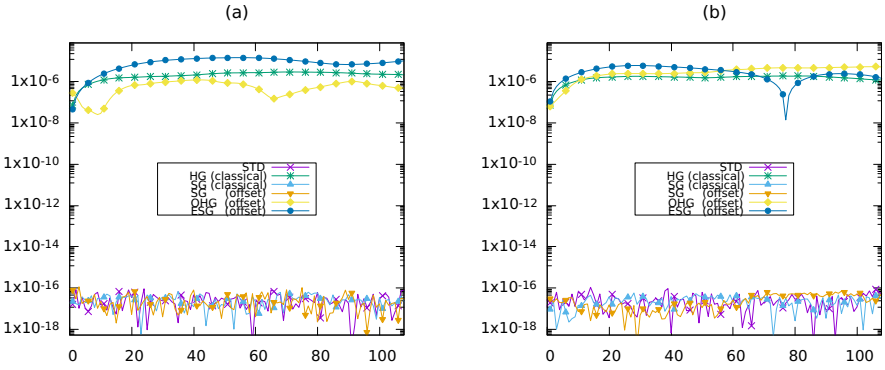

Figure 4. Non-linear Landau damping: Momentum history $\epsilon_{\mathcal{P}_x}(t)$ (a), $\epsilon_{\mathcal{P}_y}(t)$ (b).

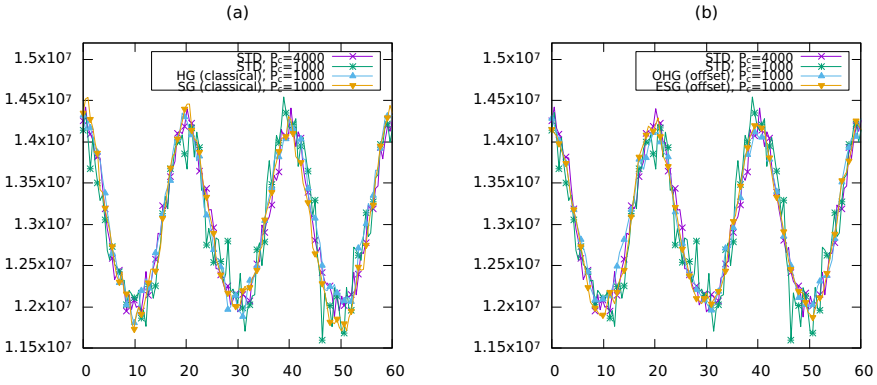

Figure 5. Non linear Landau damping: Density profile of the electron density (as a function of y) at $t = 6.3\omega_p^{-1}$ and $x = \frac{L}{2}$.

optimal precision and reduce the particle sampling error to a value comparable to the grid based error. This outlines an important characteristic of PIC methods: the grid based error is marginal compared to the particle error. This proves that gains may be expected from numerical methods with a better control of the statistical noise, hence the interest for sparse grid reconstructions.

Note that for sparse grid methods, the particle sampling error decreases with the mesh refinement but an estimated mean number of particles as stated by equations (94)-(95) remaining constant. For a refined grid with 128×128 cells, the amount of statistical noise of the HG scheme with $P_c = 500$ is lower to that of the STD scheme run with $P_c = 1000$. This amounts to a total of number of particles equal to 1.28×10^6 for the sparse method (see table 3 for the value related to $P_c = 1000$), which is 12 times less compared to the 1.64×10^7 particles used for the standard method.

The second series of simulation for the non-linear Landau damping is dedicated to the time evolution of the perturbation. First, the conservation of the total momentum is investigated for the different methods. To this end, let us introduce the following error for the momentum:

$$\epsilon_{\mathcal{P}}(t) := \frac{1}{N}\sum_{p=1}^{N} \frac{m_e \mathbf{v}_p(t_0) - m_e \mathbf{v}_p(t)}{m_e v_{th}}, \tag{98}$$

where $\mathbf{v}_p(t)$ is the velocity of the p^{th} particle at time t and $v_{th} := \sqrt{2q_eT_e/m_e}$ is the thermal velocity of the electrons. The default of momentum conservation is represented as a function of time in figure 4 (a), (b) with $P_c = 500$. As predicted by the propositions 3.13 and the remark 3.16 the total momentum is exactly conserved (to machine precision $\approx 10^{-16}$) for the SG with any of the classical combination technique or the offset combination technique, as well as the STD scheme. The conservation default for the HG, OHG and ESG schemes (see remark 3.14) is observed to remain marginal ($\approx 10^{-6}$) and bounded independently of time.

The projection onto the Cartesian grid and a section in the x-direction of the electron density are proposed in figures 5, 6 after two periods of oscillation of the electric field (at time $T_2 = 6.3\omega_p^{-1}$) for the different configurations of table 3. Since the density is never projected onto the Cartesian grid within the SG and ESG schemes, we perform an interpolation on the Cartesian grid according to the combination technique for the diagnostics.

First, it appears that the reduction of the numerical noise is manifest for all the methods using sparse grid reconstructions. It is an essential property since, this error, due to the undersampling of the distribution function, is the most detrimental in the precision of numerical methods. This better control of the numerical noise is obvious on the x-section plots displayed on figure 5. Though the estimated mean number of particles per cell is equal to 1000 for the HG (classical combination), SG (classical combination), OHG (offset combination) and ESG (offset), the magnitude of the dispersion is observed to be comparable to that of the STD scheme with 4000 particles per cell which amounts to total number of particles 25 times greater (see table 3). It is also noticeable that sparse grid approximations do not introduce too much numerical diffusion, the extrema of the numerical approximations being comparable whatever the scheme. Second, the grid-based error can be

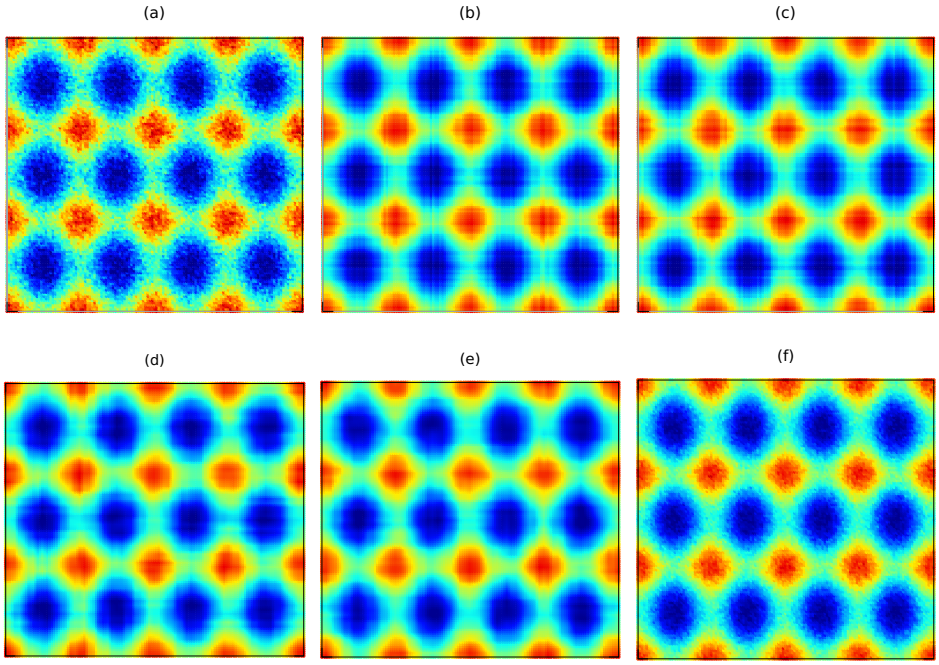

Figure 6. Non linear Landau damping: Electron density at $t = 6.3\omega_p^{-1}$ for the STD (a), HG (classical) (b), SG (classical) (c), ESG (offset) (d), OHG (offset) (e), STD (f) schemes; grid with 128×128 cells, $P_c = 1000$ (a), (b), (c), (d), (e), $P_c = 4000$ (f).

observed, particularly on the plots of the SG and HG methods. This error reproduces the patterns of the coarsest grid levels. This error is specific to sparse grid approximations of the density and analysed to be dominated by the $\mathcal{G}_n^{\times}$ grid-based component scaling with $\mathcal{O}(\log_2(h_n^{-1})h_n^2)$. This latter term results from the accumulation of error on the different levels of sub-grids and is reduced thanks to the offset combination technique (see remark 3.15). The smearing of the grid structure on the error plots related to the computations performed with the offset combination technique can be observed on figure 6. Indeed, in these computations the number of sub-grids considered for the reconstruction is reduced by taking $n_{sg} < n$ (from $2n - 1 = 13$ sub-grids to $2n_{sg} - 1 = 7$ sub-grids). The sub-grids considered in the combination are detailed in the example 2. The control of the numerical noise (with approximately the same number of total particles), though expected deteriorated, due to the use of more refined grids compared to the original methods, remains very effective improving significantly the quality of the numerical results. For these methods, still a good control of the numerical diffusion shall be pointed out. Similarly, the increase of the grid-based component $\mathcal{G}_n^{\|}$ being set by the trade-off reveals to remain marginal on the precision of the numerical approximation.

4.3. **Diocotron instability.** In this test case, we consider a hollow profile in the electron distribution, confined by a uniform magnetic field $\mathbf{B}$ [30], with the following

Maxwellian distribution of electrons :

$$\tilde{f}_e(\mathbf{x},\mathbf{v}) = \frac{\gamma}{0.03L(2\pi)^2} e^{-\frac{\left(\left\|\mathbf{x}-\frac{L}{2}\right\|_2-\frac{L}{4}\right)^2}{2(0.03L)^2}} e^{\frac{-\|\mathbf{v}\|_2^2}{2}}, \tag{99}$$

where $\left\|\mathbf{x}-\frac{L}{2}\right\|_2^2 = (x-\frac{L}{2})^2+(y-\frac{L}{2})^2$ and γ a normalization constant so that $\iint \tilde{f}_e(\mathbf{x},\mathbf{v})d\mathbf{x}d\mathbf{v} = 1$. The external magnetic field is considered uniform along the z-axis $\mathbf{B} = (0,0,B_z)$ ($B_z = 2.5\times10^{-5}$ T) and strong enough so that the electron dynamics is dominated by advection in the self-consistent field $\mathbf{E}\times\mathbf{B}$. The instability caused by the magnetic field deforms the initially axisymmetric electron density distribution, leading, in the nonlinear phase, to the formation of a discrete number of vortices. As we expect fine scale structure to form in the process, a high discretization in space is required to reproduce these structures. Again, this test case defines a demanding benchmark for sparse grid approximations very likely to outline the grid error introduced with these reconstructions.

Let the parameters be $L = 22\lambda_D$, $\Delta t = 0.1\omega_p^{-1}$, the system is observed at time $T_1 = 54\omega_p^{-1}$. The numericals results will be compared to the STD scheme with a grid composed of 256×256 cells and $P_c = 200$ particles per cells as indicated in table 4. The interpolations are implemented using B1-spline while B2-splines are used for the density visualization. Following steps of proof of proposition 3.8, one can see that the use of B2-spline, even restricted to the visualization of the density on the grid, provides a better representation of the density.

Table 4. Diocotron instability: Configuration of the numerical methods.

Scheme	Parameters	Grid size h_n	P_c	N	N_{Ref}/N
Ref (STD)		2^{-8} (256^2 cells)	200	2.621×10^7	1
STD		2^{-8} (256^2 cells)	40	2.621×10^6	5
OHG (classical)	$\delta_n = 2$	2^{-8} (256^2 cells)	40	1.187×10^6	11
SG (classical)		2^{-10} (1024^2 cells)	40	1.187×10^6	11
ESG, OHG (offset)	$(l^0,l^1,\delta_n) = (4,0,1)$	2^{-8} (256^2 cells)	40	1.802×10^6	7.25

The projection of the electron density onto the Cartesian grid and a section in the x-direction (at $x = \frac{2L}{3}$) at time T_1 for the different configurations of table 4 are represented in figure 7, 8. The numerical results are presented only for the OHG scheme and not for the HG scheme because the resolution of the Poisson problem for the latter is exceedingly costly in comparison to the others methods. Besides, the same accuracy is achieved with either the OHG scheme or the HG scheme, hilighting the benefit of the oversampled correction of the scheme. The discretizations of the sparse grid schemes with the classical combination technique ($h_n = 2^{-10}$, $h_{\tilde{n}} = 2^{-10}$) are chosen higher than the standard ones ($h_n = 2^{-8}$) because the sparse grid schemes fail to reproduce the fine-scale structures depending on cross derivative terms. Indeed, we have shown in section 3 that the grid-based error component $\mathcal{G}_n^{\times}$ scales with $\mathcal{O}(\log_2(h_n^{-1})h_n^2)$ for the sparse grid schemes (compared to $\mathcal{O}(h_n^4)$ for the standard scheme).

Despite the use of a more refined grid discretization, we observe on the plots of the section in the x-direction (figure 8 (a)) that the OHG and SG schemes with the classical combination technique still fail to reproduce correctly the fine-scale structure of the density. Indeed, where the solution has steep gradients ($y \approx 6$,

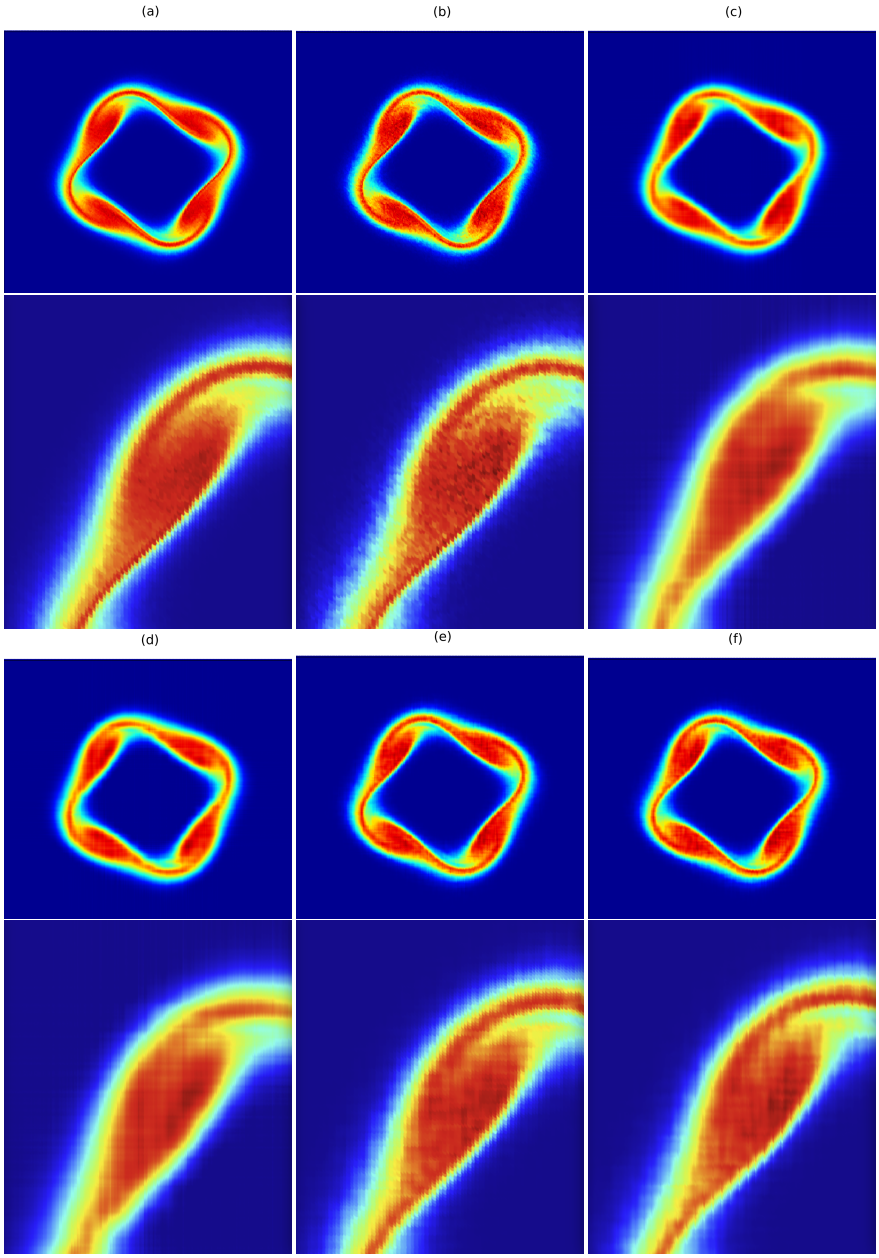

Figure 7. Diocotron instability: Electron density for the STD (a,b), OHG (classical) (c), SG (classical) (d), ESG(offset) (e), OHG (offset) (f) schemes at $t = 54\omega_p^{-1}$. Zoom on the top left corner. $P_c = 200$ (a), $P_c = 40$ (b), (c), (d), (e), (f).

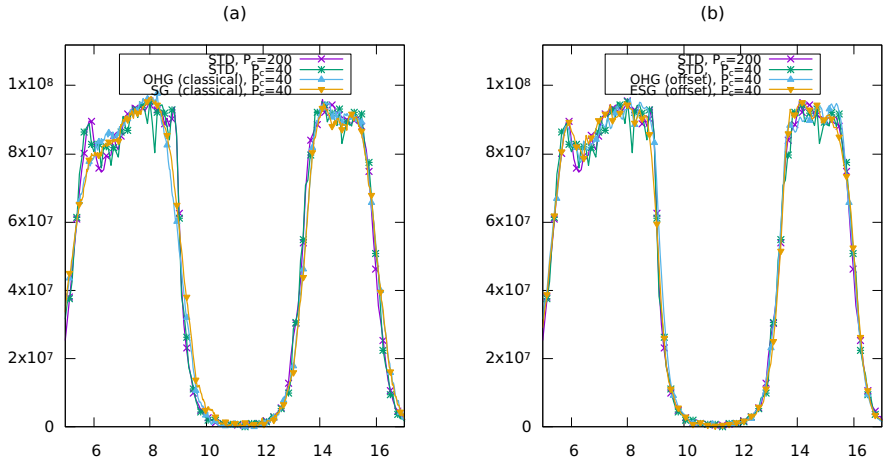

Figure 8. Diocotrom instability: Density profile of the electron density at $t = 54\omega_p^{-1}$ and $x = \frac{2L}{3}$.

$y \approx 9$ in figure 8 (a)) the sparse grid schemes show a bit of numerical diffusion. The correction of the schemes with the offset combination technique achieves a fair representation of the density and even reproduce some fine-scale structures that are faded by the statistical noise of the STD scheme with $P_c = 40$ (see zoom on figure 7). The improvement is manifest on the plot of the section in the x-direction (figure 8 (b)) where the numerical diffusion introduced by the sparse grid schemes has been mitigated. Here again the sparse grid techniques achieve an improvement on the statistical noise with the same mean number of particles per cell (and thus less total particles in the simulation) than the regular PIC approximation (see the plot of the section in the x-direction for the density in figure 8 (a), (b)). Though this test case is a very demanding benchmark for sparse grid approximations a reduction of the total number of particles is achieved (see table 4) and all the fine-scale structures appearing in the reference solution are well reproduced by the corrected schemes.

5. Conclusions

In this paper, we have presented, analysed and proposed Particle-In-Cell numerical methods embedding sparse-grid reconstructions by means of the combination technique. These methods have been numerically experienced and compared against regular PIC methods. Sparse-grid PIC approaches promise a speed-up of the method thanks to a better control of the statistical noise which entails the reduction of the particle number. A reduction of cost for the computation of the electric field is also accessible, owing to the reduced number of cells composing sparse-grids ($\mathcal{O}(\log_2(h_n^{-1})^{d-1}h_n^{-1})$ instead of $\mathcal{O}(h_n^{-d})$ for a Cartesian mesh). The analyses conducted within this document show that the approximation error may be decomposed into a particle error and a grid based error. Two components define the grid based error, namely $\mathcal{G}_n^{\parallel}$, $\mathcal{G}_n^{\times}$ with a balance between these two contributions depending on the numerical methods. The particle error, denoted $\mathcal{P}_{n,N}$, is related

to the sampling of the distribution function by particles and characterizes the dispersion of the sampling. One can conclude that the Sub-Grid (SG) and Hybrid-Grid (HG) schemes achieve both a fair representation of the density with an improved control of the statistical noise ($\mathcal{P}_{n,N}$) compared to regular PIC schemes. Nonetheless, the grid based error is deteriorated, due to the increase of the component $\mathcal{G}_n^{\times}$, depending on the solution high order cross derivatives. This increase is more substantial for three dimensional computations. Similar conclusions may be drone from the formal analysis stating the first convergence (and rate of convergence) results for the electric field sparse grid approximation established within this document (see propositions 3.11, 3.10 for the SG and HG schemes). Furthermore, the SG scheme is proved to be compliant with the conservation properties of standard PIC methods (total charge and momentum), except positivity. The offset technique is introduced to decrease the dominant component of the grid based error ($\mathcal{G}_n^{\times}$) in sparse grid PIC methods. This framework permits to tune the balance between the different components of the error and improve the quality of PIC sparse grid approximations. Besides, enhancements of the SG and HG schemes are proposed in order to improve the efficiency of sparse grid methods regarding the computation of the electric field.

The numerical experiments performed on various classical test cases, consolidate the results of the formal analyses and illustrate conclusively the gain brought by sparse grid reconstructions in particular when combined with the offset method, to improve the sampling error without introducing a significant numerical diffusion. Despite the simplicity of the implementation and the restriction to two dimensional geometries, the proposed numerical investigations provide a glimpse of PIC method implementing sparse-grid reconstructions. However the full potential of the method can only be achieved by three dimensional computations. This is strikingly illustrated by the plots of figure 9 relating the number of particles (N) required in either a 2D or a 3D computation to guarantee a similar statistical noise in both the regular and the sparse-grid PIC methods. It is manifest that the reduction of

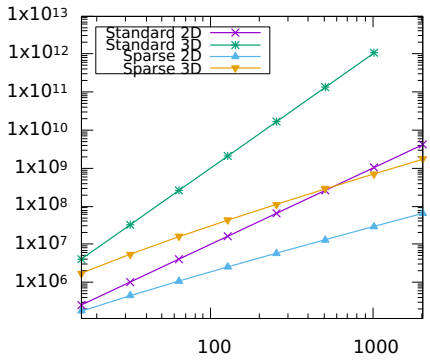

Figure 9. Number of particles required by 2D and 3D computations as a function of the number of cells (in each dimension) to recover a comparable statistical noise ($P_c = 1000$) in standard and sparse-grid PIC methods.

particles with the sparse grid schemes is significantly larger for three dimensional computations: for grid with more than 500 cells (in each dimension), the number

of particles run in the standard method for two dimensional computations is larger than that of sparse grid methods for three dimensional computations. Though these projections may be mitigated by implementation issues, the perspectives offered by the offset method together with the enhancement of the schemes introduced in this paper promise a leap forward in the efficiency of PIC numerical methods for three dimensional computations.

Acknowledgements

Clément Guillet benefits from a Université de Toulouse/Région Occitanie PhD grant.
This work has been carried out within the framework of the EUROfusion Consortium and has received funding from the Euratom research and training programme 2014-2018 and 2019-2020 under grant agreement No 633053. The views and opinions expressed herein do not necessarily reflect those of the European Commission.
This work has been supported by a public grant from the "Laboratoire d'Excellence Centre International de Mathématiques et d'Informatique" (LabEx CIMI) overseen by the French National Research Agency (ANR) as part of the "Investissements d'Avenir" program (reference ANR-11-LABX-0040) in the frame of the PROMETEUS project (PRospect of nOvel nuMerical modEls for elecTric propulsion and low tEmperatUre plaSmas).
Support from the FrFCM (Fédération de recherche pour la Fusion par Confinement Magnétique) in the frame of the SPARCLE project (SParse grid Acceleration for the paRticle-in-CelL mEthod) is also acknowledged.
Jacek Narski was supported by the ANR project MUFFIN (ANR-19-CE46-0004).
Clément Guillet is grateful to Marc Chung-To-Sang for his remarks, corrections and fruitful discussions.

References

[1] L F Ricketson and A J Cerfon. Sparse grid techniques for particle-in-cell schemes. Plasma Phys. Control. Fusion, 59(2):024002, February 2017.
[2] Sriramkrishnan Muralikrishnan, Antoine J. Cerfon, Matthias Frey, Lee F. Ricketson, and Andreas Adelmann. Sparse grid-based adaptive noise reduction strategy for particle-in-cell schemes. Journal of Computational Physics: X, 11:100094, June 2021.
[3] John M. Dawson. Particle simulation of plasmas. Rev. Mod. Phys., 55(2):403–447, April 1983. Publisher: American Physical Society.
[4] Charles K Birdsall and Dieter Fuss. Clouds-in-clouds, clouds-in-cells physics for many-body plasma simulation. Journal of Computational Physics, 3(4):494–511, April 1969.
[5] Eastwood Hockney. Computer Simulation Using Particles. SIAM Rev., 25(3):425–426, July 1983. Publisher: Society for Industrial and Applied Mathematics.
[6] R. D. Sydora. Low-noise electromagnetic and relativistic particle-in-cell plasma simulation models. Journal of Computational and Applied Mathematics, 109(1):243–259, September 1999.
[7] Pierre Degond, Fabrice Deluzet, and David Doyen. Asymptotic-preserving Particle-In-Cell methods for the Vlasov-Maxwell system near quasi-neutrality. arXiv:1509.04235 [physics], September 2015. arXiv: 1509.04235.
[8] Laurent Garrigues, Gwénaël Fubiani, and Jean-Pierre Boeuf. Negative ion extraction via particle simulation for fusion: critical assessment of recent contributions. Nuclear Fusion, 57(1):014003, January 2017. Publisher: IOP Publishing.
[9] G. Fubiani, L. Garrigues, J. P. Boeuf, and J. Qiang. Developpment of a hybrid MPI/OpenMP massivelly parallel 3D particle-in-cell model of a magnetized plasma source. In 2015 IEEE International Conference on Plasma Sciences (ICOPS), pages 1–1, May 2015. ISSN: 0730-9244.

[10] Alexander Philippov and Anatoly Spitkovsky. Ab-initio pulsar magnetosphere: three-dimensional particle-in-cell simulations of axisymmetric pulsars. ApJ, 785(2):L33, April 2014. arXiv: 1312.4970.

[11] R. E. Denton and M. Kotschenreuther. {delta}f Algorithm. Technical Report DOE/ET/53088-629; IFSR-629, Texas Univ., Austin, TX (United States). Inst. for Fusion Studies, November 1993.

[12] C.K. Birdsall and A.B Langdon. Plasma Physics via Computer Simulation. CRC Press, 0 edition, October 2018.

[13] Salimou Gassama, Éric Sonnendrücker, Kai Schneider, Marie Farge, and Margarete Domingues. Wavelet denoising for postprocessing of a 2D Particle - In - Cell code. http://dx.doi.org/10.1051/proc:2007013, 16, January 2007.

[14] Hans-Joachim Bungartz and Michael Griebel. Sparse grids. Acta Numerica, 13:147–269, May 2004.

[15] Jochen Garcke. Sparse Grids in a Nutshell. In Jochen Garcke and Michael Griebel, editors, Sparse Grids and Applications, volume 88, pages 57–80. Springer Berlin Heidelberg, Berlin, Heidelberg, 2012. Series Title: Lecture Notes in Computational Science and Engineering.

[16] Thomas Gerstner and Michael Griebel. Numerical integration using sparse grids. Numerical Algorithms, 18(3):209, January 1998.

[17] Hans-Joachim Bungartz and Stefan Dirnstorfer. Higher Order Quadrature on Sparse Grids. In Marian Bubak, Geert Dick van Albada, Peter M. A. Sloot, and Jack Dongarra, editors, Computational Science - ICCS 2004, Lecture Notes in Computer Science, pages 394–401, Berlin, Heidelberg, 2004. Springer.

[18] Michael Griebel. Adaptive sparse grid multilevel methods for elliptic PDEs based on finite differences. Computing, 61(2):151–179, June 1998.

[19] Michael Griebel. Parallel Multigrid Methods on Sparse Grids. In W. Hackbusch and U. Trottenberg, editors, Multigrid Methods III, pages 211–221. Birkhäuser Basel, Basel, 1991.

[20] Michael Griebel. The combination technique for the sparse grid solution of pde's on multiprocessor machines. Parallel Process. Lett., 02(01):61–70, March 1992. Publisher: World Scientific Publishing Co.

[21] H.-J. Bungartz, M. Griebel, D. Röschke, and C. Zenger. Pointwise Convergence Of The Combination Technique For Laplace's Equation. East-West J. Numer. Math, 2:21–45, 1994.

[22] Antoine Cerfon and Lee Ricketson. Sparse Grid Particle-in-Cell Scheme for Noise Reduction in Beam Simulations. In 13th International Computational Accelerator Physics Conference, May 2019.

[23] L. Garrigues, B. Tezenas du Montcel, G. Fubiani, F. Bertomeu, F. Deluzet, and J. Narski. Application of sparse grid combination techniques to low temperature plasmas particle-in-cell simulations. I. Capacitively coupled radio frequency discharges. Journal of Applied Physics, 129(15):153303, April 2021. Publisher: American Institute of Physics.

[24] L. Garrigues, B. Tezenas du Montcel, G. Fubiani, and B. C. G. Reman. Application of sparse grid combination techniques to low temperature plasmas Particle-In-Cell simulations. II. Electron drift instability in a Hall thruster. Journal of Applied Physics, 129(15):153304, April 2021. Publisher: American Institute of Physics.

[25] C. Reisinger. Analysis of linear difference schemes in the sparse grid combination technique. 2007.

[26] C. Pflaum. Convergence of the Combination Technique for Second-Order Elliptic Differential Equations. 1997.

[27] F. Filbet and E. Sonnendrücker. Numerical methods for the Vlasov equation. In Franco Brezzi, Annalisa Buffa, Stefania Corsaro, and Almerico Murli, editors, Numerical Mathematics and Advanced Applications, pages 459–468. Springer Milan, Milano, 2003.

[28] Janos Benk and Dirk Pflüger. Hybrid parallel solutions of the Black-Scholes PDE with the truncated combination technique. In 2012 International Conference on High Performance Computing Simulation (HPCS), pages 678–683, July 2012.

[29] Nicholas A. Krall and Alvin W. Trivelpiece. Principles of Plasma Physics. American Journal of Physics, 41(12):1380–1381, December 1973. Publisher: American Association of Physics Teachers.

[30] J. Petri. Non-linear evolution of the diocotron instability in a pulsar electrosphere: 2D PIC simulations. A&A, 503(1):1–12, August 2009. arXiv: 0905.1076.

Appendix A. Appendix

Proof of lemma 3.4. Let $\mathbf{l} = (l_1, l_2)$, because $h_{l_1} h_{l_2} = h_{|\mathbf{l}|_1}$, one gets:

$$f_n^m(\mathbf{x}) - f(\mathbf{x}) = \underbrace{\sum_{\mathbf{l}\in\mathcal{L}(n,0)} (f_{\mathbf{l}}^m(\mathbf{x}) - f(\mathbf{x}))}_{n \text{ terms}} - \underbrace{\sum_{\mathbf{l}\in\mathcal{L}(n,1)} (f_{\mathbf{l}}^m(\mathbf{x}) - f(\mathbf{x}))}_{n-1 \text{ terms}}$$

$$= (Nh_n)^{-\frac{1}{2}} \left((h_1)^{-\frac{1}{2}} \sum_{\mathbf{l}\in\mathcal{L}(n,0)} \zeta_{1,2}(\mathbf{x}; h_{l_1}, h_{l_2}) - \sum_{\mathbf{l}\in\mathcal{L}(n,1)} \zeta_{1,2}(\mathbf{x}; h_{l_1}, h_{l_2}) \right).$$

Eventually, using the boundedness of the functions $\|\zeta_{1,2}(\cdot; h_{l_1}, h_{l_2})\|_\infty \leq \kappa$:

$$|f_n^m(\mathbf{x}) - f(\mathbf{x})| \leq \kappa \left(\left(\sqrt{2} + 1 \right) n - 1 \right) (Nh_n)^{-\frac{1}{2}}. \quad (100)$$

□